



Microtremor array method using spatial autocorrelation analysis of Rayleigh-wave data

Koichi Hayashi · Michael W. Asten · William J. Stephenson ·
Cécile Cornou · Manuel Hobiger · Marco Pilz · Hiroaki Yamanaka

Received: 10 March 2021 / Accepted: 27 September 2021 / Published online: 19 April 2022
© The Author(s) 2022, corrected publication 2022

Abstract Microtremor array measurements, and passive surface wave methods in general, have been increasingly used to non-invasively estimate shear-wave velocity structures for various purposes. The methods estimate dispersion curves and invert them for retrieving S-wave velocity profiles. This paper summarizes principles, limitations, data collection, and processing methods. It intends to enable students

and practitioners to understand the principles needed to plan a microtremor array investigation, record and process the data, and evaluate the quality of investigation result. The paper focuses on the spatial autocorrelation processing method among microtremor array processing methods because of its relatively simple calculation and stable applicability.

Highlights

1. A summary of fundamental principles of calculating phase velocity from ambient noise
2. General recommendations for MAM data collection and processing using SPAC methods
3. A discussion of limitations and uncertainties in the methods

Keywords COSMOS guidelines · Best practices · Site characterization · Earthquake site effects · Microtremor array · Spatial autocorrelation · Spatially averaged coherency · SPAC · MMSPAC · krSPAC

K. Hayashi (✉)
Geometrics/OYO Corporation, 2190 Fortune Drive,
San Jose, CA 95131, USA
e-mail: KHayashi@geometrics.com

M. W. Asten
Earth Insight, Melbourne, Australia

W. J. Stephenson
U.S. Geological Survey, Golden, CO, USA

C. Cornou
University Grenoble Alpes/CNRS/IRD/IFSTTAR,
Grenoble, France

M. Hobiger
Swiss Seismological Service (SED), ETH Zurich, Zurich,
Switzerland / Federal Institute for Geosciences and Natural
Resources (BGR), Hanover, Germany

M. Pilz
Helmholtz Centre Potsdam, GFZ German Research Centre
for Geosciences, Potsdam, Germany

H. Yamanaka
Tokyo Institute of Technology, Yokohama, Kanagawa,
Japan

1 Introduction

During the past few decades, researchers have made considerable progress towards the development of passive surface wave methods utilizing seismic ambient noise, or microtremors. Microtremor noise as used here is background seismic noise attributable to road traffic and machinery (> 1 Hz) and coastal and meteorological sources (< 1 Hz). The wave energy propagates predominantly as surface waves, both

Rayleigh waves (detectable with vertical seismic sensors) and Love waves (detectable with horizontal sensors). Although both Rayleigh- and Love-wave microtremor methods have been published, most examples (e.g., Foti et al. 2017) use vertical sensors limited to Rayleigh-wave analysis; hence, we confine discussion here to this category. We group all multi-sensor methods under the common name of microtremor array measurements (MAMs) because two-dimensional (2D) arrays are usually used for calculating phase velocity from the ambient noise. Aki (1957) first proposed the study of surface waves encoded in ambient noise and presented a theory of spatial autocorrelation, or spatially averaged coherency (SPAC).

Okada (2003) developed a large-scale MAM method based on the SPAC method in order to estimate deep shear-wave velocity (V_s) structure. Among many different methods that have been developed to retrieve surface-wave phase velocities from ambient noise, SPAC is one of the most widely used methods because of its robustness, ease of implementation, and computational efficiency. A number of review papers exist describing the theory, practical array methodology, example results of the MAM, and in particular different implementations of SPAC methods. Applications are described where the methods are used to investigate the subsurface at depth scales from a few meters to a few kilometers. Asten and Boore (2005), Boore and Asten (2008), and Stephenson et al. (2005) present comparisons by up to 14 independent groups who analyzed microtremor data in the Santa Clara Valley, California. Cornou et al. (2007) summarized results of an international blind test study of both synthetic and field data from four synthetic and four field sites. The InterPACIFIC project, funded by a consortium of European government sources, obtained detailed non-invasive passive and active seismic field measurements, plus invasive borehole studies, at three European sites representing soft sediments, firm glacial sediments, and rock (Mirandola, Italy; Grenoble, France; and Cadarache, France; respectively). In this European project, a total of 14 international groups interpreted the data, and the results were summarized in Garofalo et al. (2016a) and Garofalo et al. (2016b). Foti et al. (2017) distilled the wisdom of the multiple groups into a practical guide for future surveys. Finally, the Consortium of Strong

Motion Observation Systems (COSMOS) sponsored a review paper by Asten and Hayashi (2018; hereafter AH18) and a series of blind trials where 34 international groups interpreted microtremor data from four diverse geological sites (Asten et al. 2019a; 2021a). The results of one further international blind trial were presented at the 2021 Effects of Surface Geology on Seismic Motion Symposium (Asten 2021a, b).

This document seeks to update the SPAC methodology based on experience from the COSMOS blind trials of 2018, the results of which are summarized in Section 12.

2 Principles of the MAM technique

Because the source locations generating microtremors are generally unknown, it is challenging to determine their propagation direction and thus phase velocities of surface waves composing the microtremors. Aki (1957) proposed the SPAC method in which microtremor data acquired with an array of sensors were statistically analyzed, enabling the extraction of phase velocity. The calculation of SPAC is in principle close to the general cross-correlation of ambient noise (e.g., Wapenaar 2004). SPAC can be considered the real part of cross-correlation divided by autocorrelation in the frequency domain. Further discussion and real data examples are provided in both Appendix A and AH18 (Section 10). The essential feature of the SPAC method is the calculation of the cross-correlation or cross-spectrum for the vertical-component signal from two sensors with separation r , followed by averaging of the cross-spectra around a circular array (Fig. 1). Dividing the cross-spectrum by the square root of the product of the power spectra of the two signals derives the complex coherency. For multiple pairs of stations distributed in azimuth, an average of the complex coherencies yields the spatially averaged coherency (i.e., SPAC). We note that summation around a geometric circle is not a strict requirement; we may equally use average coherencies summed for pairs of stations around the perimeter of a polygon or pairs selected from a more complex distribution of sensors such as those shown in Fig. 2, with the only provisos being similar separation distances for each station pair and a regular distribution of azimuthal angles for the pairs of stations used in the

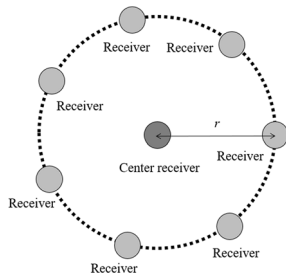


Fig. 1 SPAC calculates cross-correlations or complex coherencies between each pair of sensors with separation r and averages these around a circle. Use of three sensors on the circle is generally regarded as a minimum. A larger number of sensors provide redundancy in case of problems with a sensor or the siting of a sensor. Where sources of the microtremor surface wave energy are highly directional, the azimuthal averaging process is improved by using an odd number of sensors on the circumference, e.g., 5, 7, or 9 sensors (Okada 2006)

summation. Foti et al. (2017, supplement Fig. A2.2) further discuss attributes of different array geometries based on case histories.

When the number of station pairs sample the wavefield sufficiently in its azimuthal distribution, the real part of SPAC ($SPAC(r, \omega)$) becomes equal to a Bessel function (Aki 1957).

$$\text{Re}(SPAC(r, \omega)) = J_0\left(\frac{\omega}{c(\omega)}r\right) \tag{1}$$

where $c(\omega)$ is the fundamental mode phase velocity at an angular frequency ω . The left term of Eq. (1) is calculated from the vertical component of observed

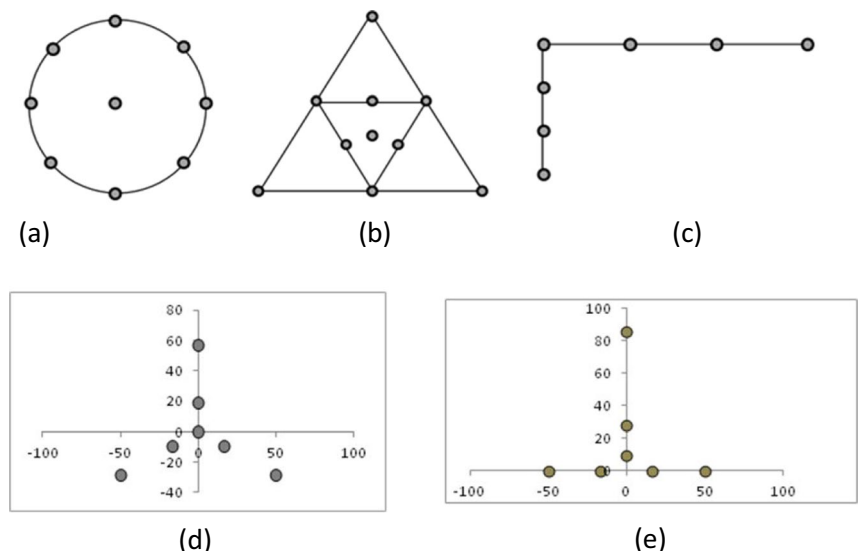
microtremor data, J_0 is the Bessel function (zero order, first kind), and r is the interstation distance. A more detailed overview of the SPAC method is given in both Appendix A and AH18 (Section 1).

In practice, the phase velocity is calculated by comparing the theoretical relationship in Eq. (1) with the measured SPAC and adjusting the phase velocity $c(\omega)$ to minimize the error. The velocity which minimizes this error can be considered the phase velocity at the angular frequency ω . The imaginary part of the $SPAC(r, \omega)$ ideally goes to zero in the directional average of ambient noise; the non-zero imaginary part can be used in an assessment of azimuthal distribution of the wavefield, in assessment of statistical noise in the SPAC data (Asten 2006), and as an additional control on phase velocity estimation (Cho 2020).

We can compare the SPAC Bessel functions in Eq. (1) against either the angular frequency, ω , or against the sensor separation, r (if there are multiple sensor separation distances). The SPAC against the angular frequency ω generally does not take the shape of a Bessel function because the phase velocity $c(\omega)$ is a function of frequency. Conversely, the SPAC against the sensor separation, r , always takes the shape of a Bessel function. Okada et al. (1997) named the latter plotting method extended spatial autocorrelation (ESAC or ESPAC).

SPAC, as defined in Eq. (1), can ideally only be applied to isotropic arrays (commonly where the inter-station sensor spacing is less than 10% difference among the averaged sensor pairs), such as

Fig. 2 Examples of array geometries which have been commonly used for microtremor studies using SPAC analysis. (Modified from AH18). **a** Circular shape. **b** Nested triangular shape. **c** L-shape. **d** Sparse nested triangles (sizes increase x3). **e** Common-base nested triangles (sizes increase x3)



circles or triangles, and should not be applied to anisotropic (or asymmetric) arrays, such as lines or L-shapes, due to the requirement for directional averaging. However, if we assume for a particular site that microtremors come from all directions equally over a 180° azimuthal spread, the directional average in the Eq. (1) can be calculated even if arrays are anisotropic (Capon 1973). Generally, the direction of propagation of the microtremor field is not stable. Averaging microtremor data over a sufficiently long recording time may enable us to calculate the directional average of Eq. (1) correctly even if the arrays are anisotropic, such as an L-shape or T-shape.

3 Current state of practice of MAM

SPAC has been widely applied to both engineering and scientific investigations for years (see list of references in the introduction above). The depth of investigation has varied from several meters to several kilometers in many of these published studies. The method has been used in multiple international blind test studies, and the results of the tests quantitatively demonstrate a lack of agreement, which has been attributed to both differing data acquisition and processing techniques (e.g., Asten and Boore 2005; Garofalo et al. 2016a; b; Asten et al. 2021a). An international committee (InterPACIFIC) tasked with reviewing active and passive surface wave methods summarized the data acquisition and processing of SPAC (Foti et al. 2017). This document seeks to update the SPAC methodology based on experience from the COSMOS blind trials of 2018 (results summarized in Section 12 and more fully in Asten et al. 2019a; 2021a). A wide range of different types of seismometers are commercially available, and multiple processing software packages are available, both free and for purchase (e.g., see Table 1 of Asten et al. 2021a, and detailed data descriptions in Asten et al.

2021b), which are briefly discussed in Sections 6 and 7 of this paper.

Given the limitations on spatial and directional averaging of microtremor signals, as discussed in Section 2, the recommended field practice is to use isotropic arrays (also termed symmetric arrays) as a default option unless prior studies have established sufficient azimuthal spread of wave energy to provide directional averaging such that Eq. (1) is a valid assumption. Section 7.3 and Asten et al. (2019a; 2021a, Site 3) show a clear example of unsatisfactory V_s interpretation where this condition was not satisfied.

4 Limitations

Like most other geophysical investigation methods, inversion of dispersion curves obtained from SPAC is generally non-unique and includes uncertainty. Both horizontal and vertical resolution decreases proportionally as investigation depth increases, and it is in part a function of the sensor spacing, as can be seen in Eq. (1). The SPAC method assumes a one-dimensional (1D) layered structure, and the applicability to 2D structure, three-dimensional (3D) structure, or complex topography has been rarely investigated; Clapgood et al. (2011; 2012) provide examples across the fault line of a rift valley in Tasmania. Chávez-García et al. (2014; 2018) studied effects on the ambient noise field of faults bounding a sedimentary basin in Greece.

The SPAC method uses ambient seismic noise, and the quality of data significantly depends on the character of the ambient noise (microtremor) wavefield at the site. The method may not work at a site with a low ambient noise level, such as a rural area or any region too remote from microtremors generated typically in urbanized areas (frequencies above ~1 Hz) or natural sources such as

Table 1 Typical data acquisition system and investigation depth for unconsolidated or weakly consolidated sediments

Seismograph	Sensor type	Natural frequency or period	Frequency range	Maximum investigation depth
Multi-channel	Geophone	>4.5 Hz	> 1 Hz	100 m
Cableless	Geophone	1 Hz or 2 Hz	>0.2 Hz	1000 m
	Broadband sensor	> 5 s	>0.1 Hz	2000 m

oceans (frequencies below ~ 1 Hz). Where ambient noise levels are low, a common solution is to drive a field vehicle back and forth in the vicinity of the array at locations sufficiently outside and azimuthally distributed around the array to satisfy the necessary assumptions of plane-wave and multi-directional seismic wave propagation across the array. Smith et al. (2013, their Fig. 5) provided an example using this approach. Roberts and Asten (2008) and Maranò et al. (2017) independently concluded that vehicle sources at a distance of twice the array radius from the array center provide a useable approximation to the desired plane-wave seismic wave field.

The data processing of SPAC assumes that either the receiver array or the direction of ambient noise propagation is isotropic. In practice, it is usually a combination of both array design and an azimuthal spread of the ambient noise direction of propagation giving sufficient averaging for SPAC methods to be effective. As a cautionary note, we advise that directionally anisotropic arrays (also called asymmetric arrays) such as linear arrays may not work where ambient noise propagation has strong directivity.

While isotropic 2D arrays are strongly recommended for SPAC analysis, there are situations where logistics, site access, or loss of a non-performing sensor results in an anisotropic array. Extensions to the SPAC method allowing use of arbitrarily asymmetric array data have been proposed, including the MSPAC method (Bettig et al. 2001) and the krSPAC method (Asten et al. 2019b). Section 10 gives an outline and example of the latter method.

5 Multiple modes of Rayleigh-wave propagation

Rayleigh waves can propagate over a solid or layered medium in multiple modes, each mode having a phase velocity dispersion curve that is frequency dependent. When Rayleigh waves are generated by surface sources and a layered earth has shear-wave velocity contrasts below about 2:1, the amplitude of the fundamental mode (R_0) dominates higher modes. However, where larger velocity contrasts occur, and especially when buried low-velocity layers exist beneath near-surface layers having higher V_s , first and second higher modes (R_1 , R_2), or even higher modes,

may carry a dominant proportion of wave energy for some frequency bands (e.g., Claprod et al. 2011; Ikeda et al. 2012; Salloum et al. 2014; Hayashi 2019).

The partition of energy between modes is dependent on three factors: the layer velocities (i.e., specific acoustic impedance contrasts), the attenuation, and the nature and depth of the wave sources (whether vertical impacts or other types of sources). If we assume that sources are from vertical impacts at the surface of the Earth and that the Earth consists of laterally uniform elastic homogeneous layers, the energy partition between different modes can be theoretically computed (e.g., Ikeda et al. 2012; Hayashi and Craig 2017), and we can define an “effective mode,” often labeled R_e . Figure 3 shows the theoretical first three Rayleigh-mode phase velocity dispersion curves (solid lines), their relative amplitude (dashed lines), and the dispersion curve for the effective mode for a high-contrast interface at 20-m depth. For most of the frequency bands of interest, the R_0 mode dominates, but between 5 and 10 Hz a significant fraction of the Rayleigh-wave energy propagates in the R_1 mode, with the result that the R_e dispersion curve separates from R_0 and shows an upward notch to higher velocities in that frequency band. It implies that an interpretation taking only the fundamental mode into account may provide incorrect velocity-depth profiles. In many field studies over high-contrast layer boundaries, observed dispersion curves show the same notched shape associated with frequency-dependent changes in energy partition between modes.

The consequence of such energy (power) partitioning between modes is typically small for studies of geological sections with small shear-wave velocity contrasts across layer boundaries (i.e., less than about 2:1). Interpretation in such cases may be achieved considering only the fundamental mode of propagation. However, when larger shear-wave velocity layer contrasts exist ($> 2:1$), correct interpretation may require analysis in terms of the “effective mode” dispersion curve (blue solid line in Fig. 3) in which the higher modes are explicitly modeled. Such analysis is not perfect since it assumes the power partition between modes follows a theoretical model for vertically acting surface sources on a laterally homogeneous earth. However, practical experience indicates it is a useful approximation when strong layer contrasts are suspected. Other exceptions may occur where energy sources are not at the surface (e.g.,

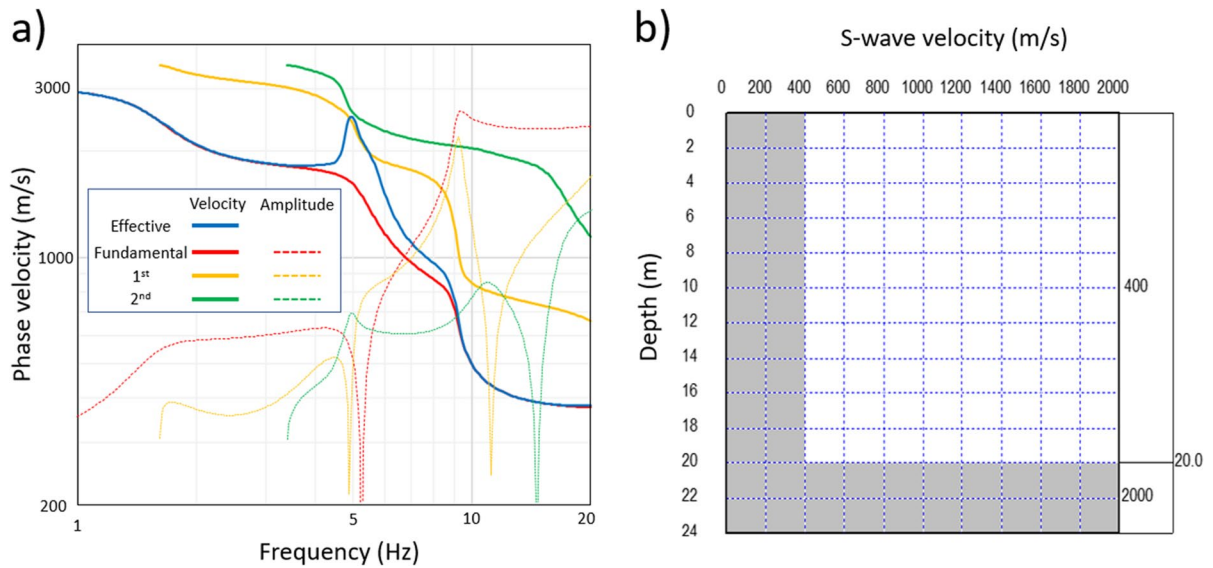


Fig. 3 **a** Example of theoretical dispersion curves for three Rayleigh modes over a high-contrast interface. Solid and dashed red, yellow, and green lines show dispersion curves and their relative amplitudes for modes R_0 , R_1 , and R_2 , respectively.

buried machinery) or when lateral changes in V_s produce mode conversions in Rayleigh waves. Foti et al. (2017, Appendix 5) provide an extensive discussion of these issues.

6 Data collection

6.1 Equipment

Two types of data acquisition systems are mainly used for obtaining microtremor array data: (1) a multi-channel seismograph system, where dozens of receivers typically are connected through multi-channel cables (wires); and (2) a wireless array of self-contained seismographs that includes a GPS clock with each sensor so that all units can be synchronized over any distance. The multi-channel seismographs generally use receivers which are velocity meters (geophones) with a natural frequency of 1 to 4.5 Hz. Wireless seismograph systems commonly use either accelerometers or velocity sensors. The multi-channel seismographs are mainly used for smaller (<100 m) arrays, and the wireless seismographs are mainly used for larger arrays (>100 m). Since the wireless seismographs are generally used for larger arrays that require

low-frequency phase velocities, broadband sensors or geophones with a low resonance frequency are used as receivers. Multi-channel seismographs have been used for exploration seismology, and many different types are commercially available. Wireless seismograph systems are becoming popular since instrumentation has become smaller and less expensive, owing to the progress of electronics. These newer systems are commonly referred to as nodal arrays. The growing availability of wireless seismographs with broadband sensors enables us to perform SPAC measurements efficiently with large seismic arrays. The choice of acquisition systems strongly depends on the noise level, geology of sites, and investigation depth. Table 1 summarizes typical data acquisition systems and achievable investigation depths over unconsolidated or weakly consolidated sediments. It is important to choose appropriate equipment and verify suitable data quality during fieldwork immediately after data collection.

6.2 Deployment

Our recommendation for passive surface wave methods is to use 2D arrays such as those shown in Fig. 2 or more generally by Foti et al. (2017) and AH18

because SPAC essentially depends on directional averaging of the wave field, as mentioned in Section 2. The circular array gives the most effective azimuthal averaging, especially where an odd number of stations are used on the circle circumference (Okada 2006). Poggi et al. (2017) give examples of arrays consisting of multiple circular arrays applied to challenging stiff soil sites in the Alps. For more general applications, the sparse nested or common-base triangles are the most efficient geometry since these give sufficient azimuthal averaging in most cases. Zhang and Pankow (2021) give examples of how square sub-arrays extracted from a larger grid of stations allow the SPAC method to be applied over a region, with the result that a quasi-3D geological model can be constructed from the set of 1D interpretations from each sub-array. In areas of restricted access, L-shaped arrays can also be useful. In some cases, useful SPAC data can be obtained with a linear array or even a two-station array (Hayashi 2009). However, it should be noted that linear arrays require the propagation of ambient noise to be omni-directional over 180° of azimuth, and that 2D regular arrays are generally desirable.

Array size (or maximum receiver spacing) and the maximum wavelength obtained from SPAC are directly related. As a rule of thumb, the maximum wavelength is generally between 2 and 4 times the array size regardless of array size and shape (Cornou et al. 2007; Hayashi 2019). It is generally agreed that the maximum penetration depth of surface wave methods is roughly in the range of 1/2 to 1/4 of maximum wavelength (e.g., Xia et al. 1999). We therefore conclude that the approximate penetration depth of the passive surface wave methods using SPAC is between 1 and 1.5 of the maximum receiver separation for a given array (Foti et al. 2017). It should be noted that the penetration depth of SPAC strongly depends on the noise level and geology of sites. The penetration depth might be much shallower compared with the maximum receiver spacing at low noise level sites. The use of broadband sensors and long record length are necessary to assure low-frequency data and a large penetration depth.

The minimum penetration depth (or near-surface resolution) achievable with SPAC is dependent on the shortest wavelength resolvable. The short wavelength limit is in part dependent on the useable spectral bandwidth in the Rayleigh-wave data, which in turn

is dependent on the choice of the SPAC software processing algorithm used (Asten et al. 2021a).

We propose the guidelines for minimum and maximum depths of investigation D_{\min} , D_{\max} , to be

$$\begin{aligned} D_{\min} &= \lambda_{\min}/3 = V/(3 \cdot f_{\max}), \\ D_{\max} &= \neg\lambda_{\max}/2 = V/(2 \cdot f_{\min}) \end{aligned} \quad (2)$$

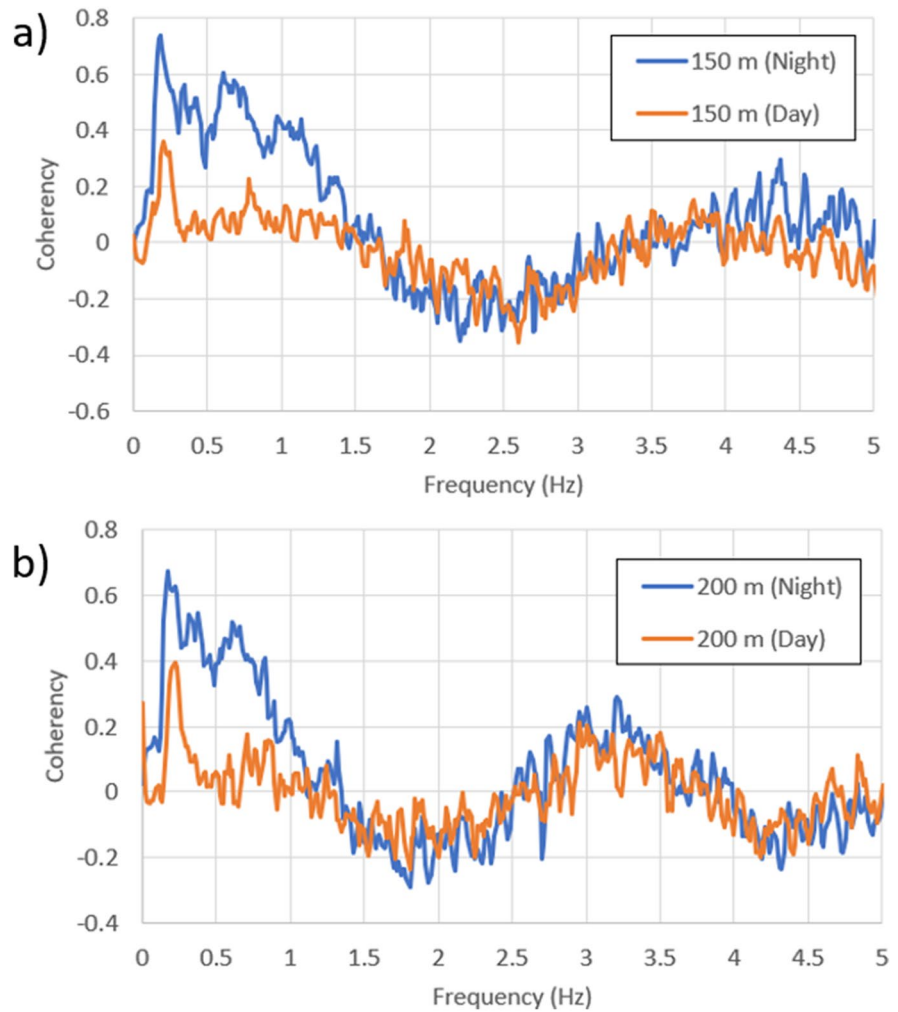
where λ_{\min} and λ_{\max} are the minimum and maximum wavelengths, f_{\min} and f_{\max} are the minimum and maximum frequencies provided by SPAC analysis respectively, and V is the phase velocity observed at a given f_{\min} or f_{\max} . Further discussion is provided in AH18 Section 3.

6.3 Recording

Longer recording time (and thus more data) is better for statistical analysis in SPAC. However, the need for long data acquisition times decreases the field efficiency of the method; therefore, recording microtremor data with an appropriate data length is a very important factor in practical survey design. Several experimental studies (i.e., Hayashi et al. 2006; Hayashi 2009; 2019) demonstrate that 10 to 20 min of data are usually enough for arrays with a spacing of less than 100 m. The record length needs to be increased for larger array sizes, although data quality varies between sites. Typical recording times are 30 to 40 min for an array size of several hundred meters, and a couple of hours for arrays larger than 1 km. Data longer than several hours usually does not improve data quality significantly; provided sources of microtremor energy are constant.

However, some surveys such as at urban sites can have significant problems with local seismic sources (e.g., machinery) existing within an array; these can lead to near-field nonplanar wave propagation resulting in low interstation coherencies. Figure 4 shows an example where nighttime recording is strongly preferable due to absence of local daytime sources. Another instance where long recordings may be desirable is at low-noise remote sites where energy sources for microtremor energy are sparse. Schramm et al. (2012) give such an example where the most useful microtremor energy in the desert environment over 24 h was from late afternoon recordings; that result may have been associated with increased wind energy late in the day. These examples illustrate exceptional

Fig. 4 Comparison of observed coherencies obtained during daytime and nighttime in an urban area (downtown Seattle, WA, USA), using receiver distances of **a** 150 m and **b** 200 m. Coherencies observed in the nighttime (blue lines) for low frequencies (<1.5 Hz) are clearly larger than those observed in the daytime (orange lines)



situations where recording overnight may be advantageous if site logistics can be arranged.

7 Data processing

7.1 Phase velocity calculation from microtremor waveforms

Two approaches are accepted for data processing steps in SPAC analysis. In the first approach, the recorded vertical-component microtremor time-series data are divided into multiple time blocks (typically a couple of minutes) that can be overlapped by a small amount of time, or by a proportion of the time block length. The time series of all stations must be aligned to a common time origin before selecting the time

blocks. As a quality-control step, selection of these blocks will typically exclude bursts of non-stationary noise, such as those from local moving vehicles. A fast Fourier transform (FFT) is applied to each time block to transform the time domain waveform data to the frequency domain. Coherencies between pairs of sensors are first calculated for each time block, and then coherencies of all time blocks are averaged for a set of sensor spacings (Appendix A). If the coherencies are averaged over many time blocks or over a sufficiently long time and over many different azimuthal pairs, it can be considered to approximate a Bessel function, as shown by Eq. (1). The processing can be done in the time domain, although most of the processing algorithms currently available use coherencies computed in the frequency domain. A more detailed overview of the SPAC method is given in Appendix A.

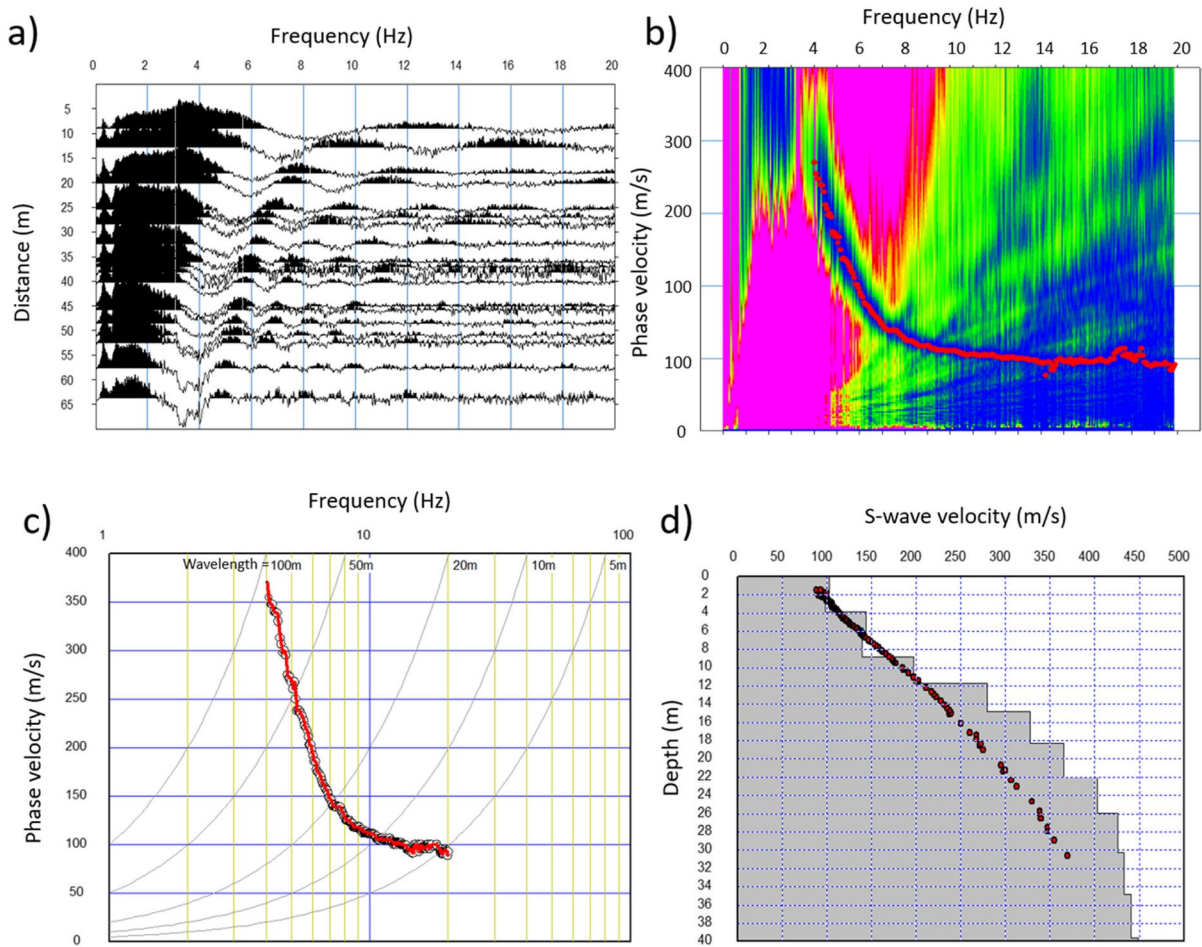


Fig. 5 Outline of processing based on SPAC. **a** Coherencies against distance (separation between receivers). **b** Phase velocity image in frequency domain. Differences of color indicate differences of error between observed coherencies and theoretical Bessel functions shown in equation Eq. (1). Blue

color indicates small error and red color indicates large error. Red dots show phase velocities that give minimum difference between both sides of Eq. (1). **c** Dispersion curve. **d** Initial velocity model together with 1/3 of wavelength (red circles) converted from observed phase velocities

In the second approach, after selection of a single long block of data (with deleterious features such as local impulsive spikes removed), perform the FFT on the single block; compute the coherency spectra for pairs of stations; and average the complex coherencies over the specified frequency windows (Asten 2006). The two approaches are equivalent.

Figure 5a shows an example of coherencies as a function of interstation sensor distance. A phase velocity can be determined at each frequency so that the difference between both sides of Eq. (1) is minimized. Figure 5b is a phase velocity image in the frequency domain that shows the error between observed coherencies and theoretical Bessel functions. This

series of phase velocities defines a dispersion curve (phase velocity-frequency observations; Fig. 5c). A velocity model for shear-wave velocity (V_s) versus depth is obtained by inversion, as described in the next sub-section.

7.2 Inversion

A V_s model is generally obtained from dispersion curves (first calculated through the waveform processing outlined in the previous section), by a non-linear inversion. Most inversions require some initial models or search areas to estimate appropriate models. These models and search areas are generally

created by a simple wavelength transformation (Xia et al. 1999), in which wavelengths are calculated from phase velocity and frequency divided by 3 and plotted as depth. Figure 5d shows an example of an initial velocity model overlain by the 1/3 wavelength-phase velocity pairs calculated from the dispersion data in Fig. 5c.

There are many non-linear inversion methods, with iterative non-linear least squares, genetic algorithms, and simulated annealing among the most prominent (e.g., Menke 1984). All inversion methods try to reduce the error between the observed and predicted phase velocities.

$$\sum_i^N (f_i^{\text{obs}} - f_i^{\text{cal}}(Vs_1, Vs_2, \dots, Vs_M))^2 = \sum_i^N (f_i^{\text{obs}} - f_i^{\text{cal}}(x))^2 \rightarrow \text{Minimum} \quad (3)$$

where Vs_1, Vs_2, \dots, Vs_M are the Vs values for the 1st, 2nd, and M th layers, respectively. N is the number of observed phase velocity data; f_i^{obs} represents phase velocities obtained from observed waveform data; and f_i^{cal} is the set of fundamental-mode theoretical phase velocities for the Vs model. In the non-linear least squares method, the iterative process changes the Vs until a good fit is obtained between the observed and calculated phase velocities. Theoretical dispersion curves are generally calculated by a matrix method (e.g., Saito and Kabaswa 1993). Since this is the most commonly used method, we summarize the details of the iterative non-linear least squares method in Appendix B.

An alternative approach to fitting observed and dispersion curves is to fit observed and predicted SPAC curves directly. As with the previous method, the model SPAC curve requires computation of a model dispersion curve for a specified layered earth, but it has some advantages in avoiding the highly non-linear step of obtaining an observed phase velocity dispersion curve from a SPAC spectrum. Known as multi-mode SPAC, MMSPAC, or direct-fitting SPAC, the approach may have an advantage in inverting Eq. (1) when, by definition, the inverse Bessel function is multi-valued (Asten et al. 2004; Asten 2006). Figure 6 illustrates the alternative processing and inversion paths used by ESAC or SPAC dispersion curve and MMSPAC direct-fitting methods. Zhang et al. (2019) provides a detailed discussion of inversion methodology for the direct fitting method. AH18 Section 5 provides a more detailed discussion

of both processing paths. Section 9 provides field examples demonstrating both approaches.

The calculation of theoretical dispersion curves requires P-wave velocity (Vp) and density in addition to Vs . Since the effects of Vp and density in the dispersion calculation are much smaller compared to Vs (Xia et al. 1999), Vp and density are commonly automatically changed with Vs or set to reasonable constant values. In the absence of other information, Vp above groundwater level is often assumed to be double Vs , and beneath the groundwater level Vp may be set to reasonable constant values, or it may be automatically changed based on an empirical relationship (e.g., Kitsunezaki et al. 1990; AH18 Section 3). Vp - Vs relationship shown in Kitsunezaki et al. (1990) can be written as,

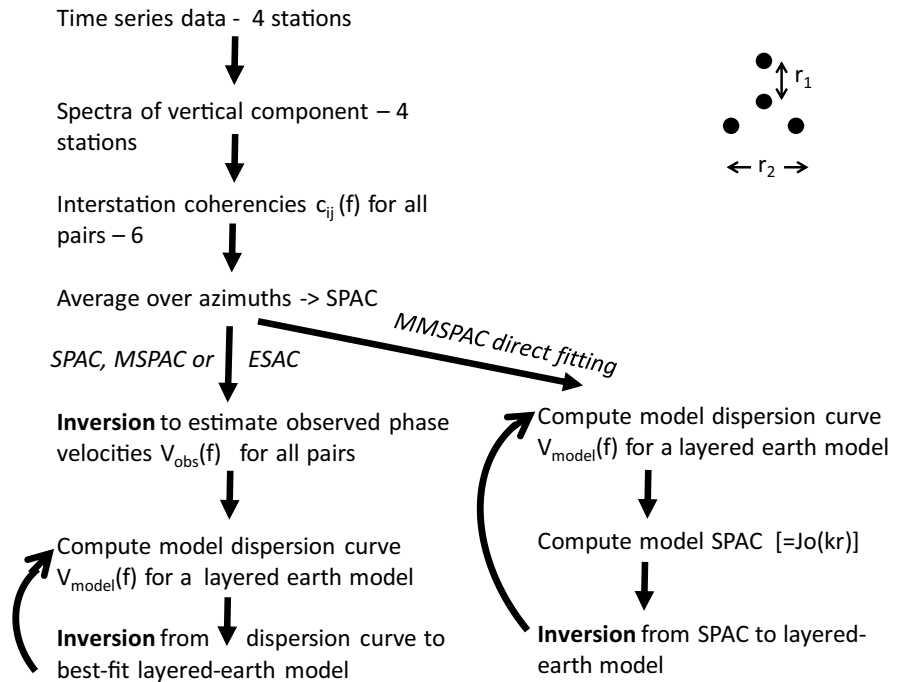
$$Vp = 1.11 \cdot Vs + 1290(\text{m/s}) \quad (4)$$

Similarly, density may be assumed, or it may be automatically changed based on empirical relationships (e.g., Ludwig et al. 1970).

The choice of method for Vp and density is not critical because dispersion curves are generally insensitive to these parameters. An exception applies at the water table; because Vp above and below the groundwater level shows a large change in unconsolidated soil, it follows that the location of the water table may have a large effect on an estimated Vs model in soft sediments. In such cases, it is desirable to obtain reliable groundwater information from other investigations, such as borings. If there is no reliable groundwater information, it may be better to assume the water level to be at the ground surface. Shallow groundwater implies high shallow Vp , which results in interpretations of lower Vs ; these lower values can be considered conservative estimates from an engineering point of view.

Most active and passive surface wave methods assume that dispersion curves are dominated by the fundamental mode (R_0). The higher modes may, however, dominate in several types of velocity structures, such as in situations where a high-velocity layer overlies a low-velocity layer, or where high-velocity layers are embedded between low-velocity layers. It is therefore necessary to take the higher modes into account in the inversion of dispersion curves in these cases (see previous section).

Fig. 6 Alternative processing and inversion paths used by ESAC or SPAC dispersion curve methods (at left) and by MMSPAC direct-fitting methods (at right). A triangular array (top right) provides SPAC spectra for two station separations r_1 and r_2 , which can be inverted or fitted simultaneously using either of the two processing paths. (Modified from AH18)



Analysis including higher modes remains an active research topic. In SPAC analysis, the effective mode (R_e) introduced in Section 5 is often used to account for higher modes (e.g., Obuchi et al. 2004; Ikeda et al. 2012; Foti et al. 2017 Appendix 5). The effective mode is the weighted average of the fundamental and higher modes. SPAC analysis including higher modes can be written using the effective mode of surface waves $C_s(\omega)$.

$$J_0 \left\{ \frac{\omega r}{C_s(\omega)} \right\} = \frac{\sum_{i=0}^n p_i(\omega)}{P(\omega)} J_0 \left\{ \frac{\omega r}{C_i(\omega)} \right\} \quad (5)$$

where $p_i(\omega)$ is the power fraction of the i th mode of the surface waves, n is the number of modes, and ω is the angular frequency. $P(\omega)$ is the sum of power of all modes. $C_i(\omega)$ is the phase velocity of the i th mode of surface waves, and r is the receiver spacing.

To calculate the effective mode phase velocity ($C_s(\omega)$), medium response and phase velocity ($C_i(\omega)$) are calculated by the matrix method. The medium response can be considered relative amplitude among fundamental and higher modes of surface waves used as the power ($p_i(\omega)$) in Eq. (5). In SPAC processing, observed coherencies, or the left-hand side of Eq. (1), are calculated from ambient noise, and

the effective mode phase velocity ($C_s(\omega)$) is used to calculate the Bessel function (the right-hand side of Eq. 1) instead of the fundamental mode phase velocity ($c(\omega)$). Figure 7 shows an example of a dispersion curve including higher modes and an estimated velocity model. The fundamental mode and higher modes up to the 5th mode were considered in the calculation of the theoretical dispersion curves. Observed phase velocities are shown as white circles with a solid red line, and the modeled effective mode R_e phase velocities are shown as yellow circles. Solid and broken lines indicate fundamental and higher mode theoretical dispersion curves and their relative amplitude (response of the medium). We can see that a bump on the dispersion curve around a frequency of 1 Hz is due to the relatively large amplitude of the first higher mode. We cannot simply apply Eq. (5) to the SPAC data from different receiver spacings. Instead, a direct-fitting method described below enables us to compare coherencies and Bessel functions for different receiver spacings individually. Additional examples of fitting observed and model SPAC curves using assumed R_0 and R_e propagation are provided in Sections 9 and 10, and in AH18 (their Figs. 4 and 7).

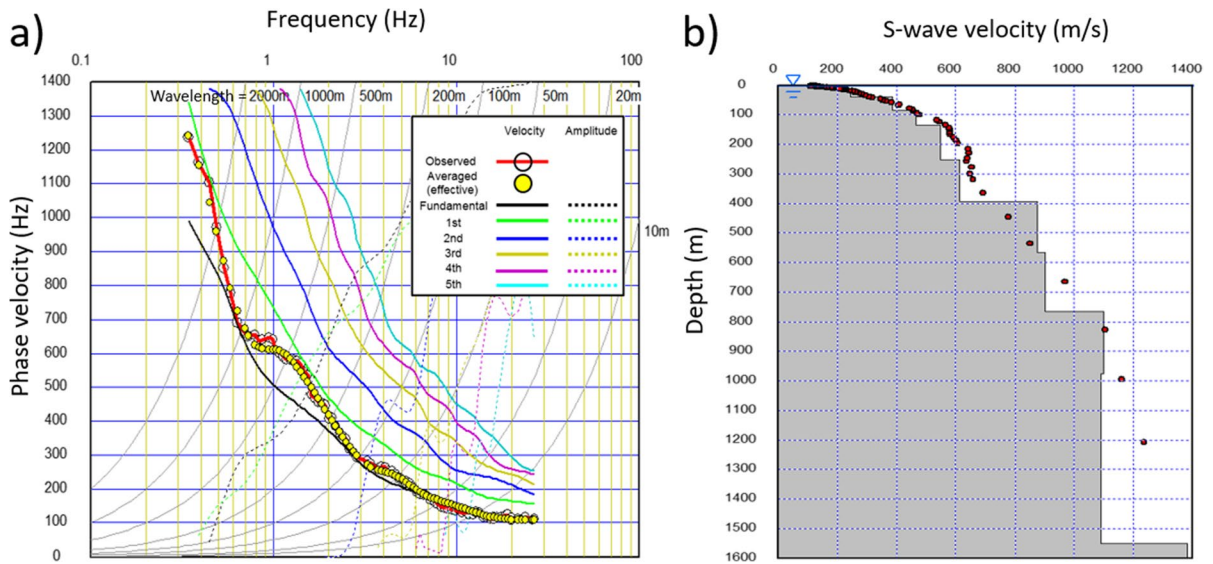


Fig. 7 **a** Example of an observed dispersion curve (solid red line) together with model (effective mode R_c) dispersion curves (yellow circles) computed using the Rayleigh-wave fundamental and five higher modes. Solid lines indicate fundamental and higher mode model dispersion curves, and broken lines

indicate relative medium responses (e.g., Ikeda et al. 2012; Hayashi and Craig 2017). **b** The interpreted shear-wave velocity model together with the $1/3$ wavelength calculations (red circles) converted from observed phase velocities

The iterative non-linear least squares method is computationally fast and generally stable if appropriate initial models were provided. It should be noted that the method can be very easily trapped in a local minimum. The method also requires the calculation of partial differentials. Fortunately, the fundamental mode dispersion is generally continuous, and the partial differentials can be calculated. The effective mode or dispersion curves including the higher modes, however, are often discontinuous, and the calculated partial differentials may not be meaningful. In such a case, the iterative non-linear least square method cannot be applied. Global search methods, such as a Monte Carlo method (e.g., Saifuddin et al. 2018), a genetic algorithm (e.g., Yamanaka and Ishida 1996), or a simulated annealing algorithm, are often used instead of the iterative non-linear least squares method to avoid being trapped in a local minimum. The methods are computationally slow but do not require the calculation of partial differentials and can be applied to dispersion curves including higher modes (Hayashi 2019). The various inversion methods all have strengths and weaknesses, and we recommend applying several different inversion methods with

different initial models, search areas, constraints, and parameters. Among various inversion methods, we prefer the non-linear least squares method with fundamental mode of dispersion curve as the first choice since the method is relatively simple, fast, and stable. The genetic algorithm or simulated annealing with a higher mode dispersion curve may be the second choice if field data are found to include significant higher modes. MMSPEC or direct fitting SPAC can be also an alternative for taking the higher modes into account.

7.3 Uncertainty analysis

The inversion of dispersion curves obtained from SPAC is generally non-unique, like most other geophysical methods. In this section, we mainly summarize the causes and consequences of uncertainty associated with the calculation of coherencies or dispersion curves from ambient noise by SPAC methods. As mentioned earlier, SPAC requires either omni-directional noise propagation or receiver array geometry to be isotropic. Asymmetric arrays, such as a linear array, may not work where noise propagation has strong directivity. The 2D arrays shown in Fig. 5 generally provide

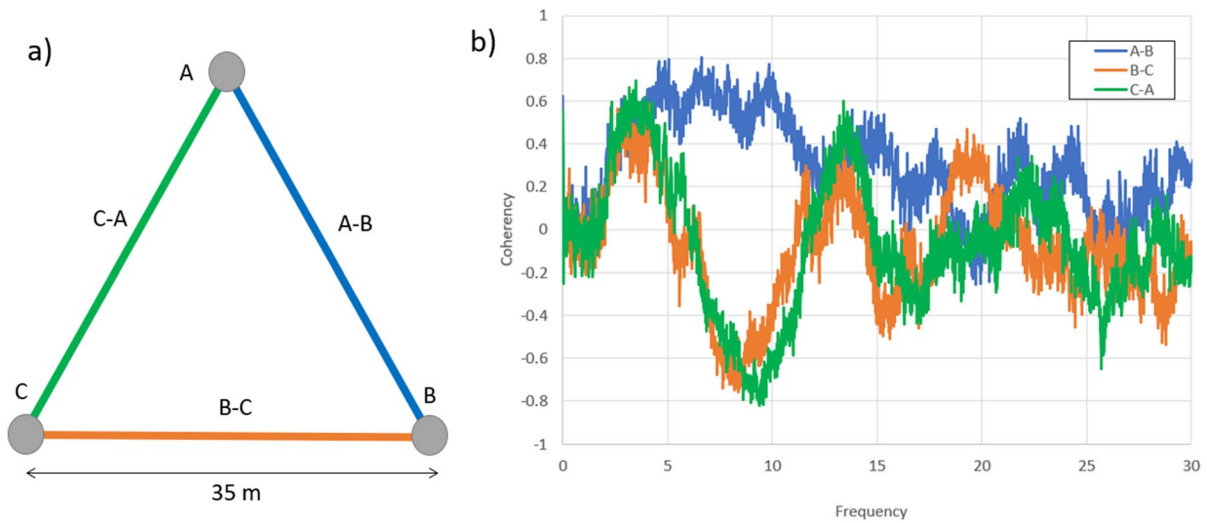


Fig. 8 Example of coherencies obtained from the noise with strong directivity (site 3 of Asten et al. 2021a). **a** Array used in data acquisition. **b** Coherency spectra calculated between

individual pairs of receivers. It appears that the ambient noise mainly propagates from bottom left to top right

reliable dispersion curves even if the noise propagation has strong directivity. Figure 8 shows an example of coherencies obtained from ambient noise with strong directivity. An equilateral triangle with four receivers is used in the data acquisition. Three coherencies are calculated between each corner and center receiver. In the ideal case, the three coherencies should be identical if the noise is isotropic. However, we see that the three coherencies have large differences, which indicates strong noise directivity. To avoid problems caused by such directivity, the use of isotropic arrays, such as circular or triangular shape shown in Fig. 2, is strongly recommended. If site access is such that only a linear array can be used, measuring with several different directions, with different time periods, or by comparing with active methods, may increase the reliability of the investigation.

Inappropriate array size or receiver spacing may decrease accuracy and reliability. Insufficient array size particularly tends to result in phase velocity estimates that are systematically underestimated at low frequencies or long wavelengths. Figure 9 shows the example of dispersion curves obtained from three different array sizes at the same site. We can see that the phase velocity tends to be biased to low values when the wavelength is longer than approximately double the array size. To avoid the problem, the use of a sufficiently large array is crucial. It is strongly

recommended to use a maximum receiver spacing larger than the depth of investigation. Sufficient ambient noise level in the frequency range of interest and the use of appropriate sensors are also important.

SPAC assumes all microtremor sources are far enough away from an array of measurements so that plane wave propagation can be assumed. Sources placed within or near the array may cause serious problems in phase velocity calculations. Traffic noise in urban areas is a typical example of such undesirable sources. The traffic noise is generally large during daytime and small during nighttime; therefore, it may be better to perform data acquisition of larger arrays at nighttime in urban areas. Figure 4 shows a comparison of observed coherencies obtained during daytime and nighttime in an urban area, and in this example, we can see that coherencies during the daytime are reduced to unusable small values for frequencies below 1.5 Hz. By contrast, coherencies from data acquired during nighttime are useable down to a frequency of 0.2 Hz.

8 Alternative data collection and processing methods

There are many different data acquisition and processing methods to estimate V_s structures from seismic

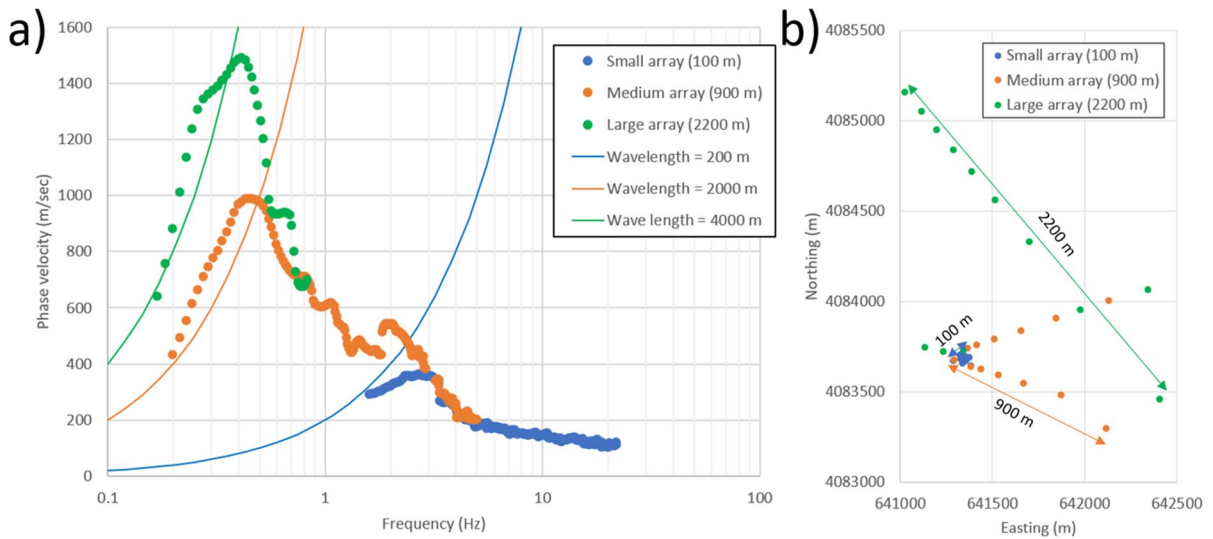


Fig. 9 Example of dispersion curves (**a**) obtained from three different size of arrays (**b**) at the same site. Solid lines in **a** indicate wavelength approximately double array sizes. Note that apparent phase velocities where the wavelength is longer

ambient noise (Table 2). Socco and Strobbia (2004) describe various modalities for the processing of seismic data in terms of surface wave analysis (like tau-p, frequency decomposition, omega-c, and frequency wavenumber). People have used SPAC and frequency wavenumber beamforming (FK) (Capon 1969) for many years. The most important advantage of FK processing over other methods is that the method can estimate propagation direction of ambient noise and can separate multiple modes of Rayleigh-wave propagation without requiring the concept of the effective mode. An important disadvantage of FK processing is that the method requires a relatively large number of sensors (at least 7, 10 to 14 preferred) compared with SPAC. Poggi et al. (2017) gave examples of the detailed study of the wave-field possible when using arrays with 19 to 30 sensors. Wathelet et al. (2018) also studied the three-component FK method with both synthetic and field data and showed its advantages in identifying multiple Rayleigh modes. AH18 (Section 9) discussed the strengths and weaknesses of the SPAC and FK methods. Seismic interferometry (SI), proposed by Wapenaar (2004), has gained popularity to calculate phase or group velocity from ambient noise array data. The SI approach allows users to calculate group velocity from data recorded by spatially aliased receiver arrays, while other methods

than 1.5 to 2 times the array size are biased by noise to low values; these must be discarded before inversion to a velocity model

generally require a spatially unaliased receiver array. A clear disadvantage of the SI method is that it requires a much longer record length of microtremors compared with SPAC. Appendix A and AH18 (Section 10) discussed similarities and differences between SPAC and SI. Cho et al. (2013) proposed a centerless circular array (CCA) method and claimed that the method could estimate phase velocities for wavelengths up to 100 times the diameter of the circular array. Louie (2001) proposed a passive surface wave method using a linear array, named the refraction microtremor (ReMi) method (see paper by Louie et al. 2021, this volume). This method is widely used to estimate average V_s down to 30-m depth (V_{s30}) for engineering purposes since the method is relatively simple and easy to carry out using conventional multi-channel seismographs.

The use of Love-wave dispersion curves, obtained from the horizontal component of ambient noise, has been proposed as a method to decrease the uncertainty of V_s inversion and increase the accuracy of a given investigation. Although numerous attempts have been made by researchers to extract Love wave dispersion curves from three-component ambient noise (e.g., Aki 1957; Yamamoto 2000; Okada 2003), the use of horizontal-component data still remains in the research and development phase. The recorded

Table 2 Data collection and processing methods to estimate V_s models from seismic ambient noise

Method	Data acquisition	Processing	Strength	Weakness	Reference
Spatial autocorrelation (SPAC)	1D/2D array	Calculate phase velocity by comparing cross-correlation (CC) in frequency domain with Bessel function (J_0)	Work with relatively small number of sensors	Impossible to calculate propagation direction	Aki 1957
Frequency wavenumber (FK) beamforming	2D array	Find maximum amplitude in vector wavenumber domain	Calculate propagation direction	Requires relatively large number of sensors (generally more than 10)	Capon 1969
Seismic interferometry	1D/2D array	Calculate phase or group velocity from time domain of CC	Calculate group velocity from spatially aliased data	Requires relatively long (at least several times compared with SPAC) ambient noise to calculate group velocity	Wapenaar 2004
Direct fitting	2D array	Compare real part of CC with Bessel function calculated from velocity model	Handle multi-modes with multi-receiver separation	Difficult to estimate initial V_s profile from SPAC	Asten et al. 2004
Centerless circular array (CCA)	2D array	Calculate phase velocity by comparing alternative CC with Bessel function ratio (J_0^2/J_1^2)	Calculate relatively long wavelength phase velocity with small array	Requires circular or triangular array	Cho et al. 2013
Refraction Microtremor (ReMi)	1D array	Pick minimum apparent velocity in tau-p domain	Simple equipment and data acquisition	Requires omni-directional ambient noise	Louie 2001

vertical component of ambient noise only consists of Rayleigh waves, whereas horizontal components consist of both Rayleigh and Love waves. It is thus necessary to estimate the Rayleigh and Love amplitude ratio to calculate Love-wave velocity, and this requirement makes the use of horizontal-component data in dispersion-curve analysis difficult.

All the data correction and processing methods summarized above have strengths and weaknesses, and blind tests such as that summarized in Section 11 suggest no microtremor array data processing method is wholly superior over other methods. The best method depends on site conditions, investigation purposes, and available resources, among other factors. We recommend applying several different processing methods to the same data and comparing the resulting dispersion curves. In this way, the uncertainty in calculating the dispersion curve can be decreased, and the reliability of the resultant V_s structures can be increased. It is important to choose array configurations to which several processing methods can be applied. Among various processing methods, we

prefer SPAC as the first choice since the method is generally robust and stable and works with a small number of sensors. FK beamforming may be the second choice if we need to estimate the direction of ambient noise propagation and if many sensors are available. SI is a useful alternative if the use of wide sensor spacings has resulted in spatially aliased data.

9 Case studies

A large number of case histories exist where MAM investigations are supplemented with three-component horizontal-to-vertical spectral ratio data (HVSr). The HVSr method is reviewed in detail by Molnar et al. (2018; 2021). We include HVSr data for the Mexico City case history discussed in this section.

The M_w 8.0 earthquake that struck Mexico City on 19 September 1985 caused severe damage although the city was 400 km from the epicenter. The main reason for this is that the city is located on a very soft sedimentary basin (Abe 1986). The distribution of

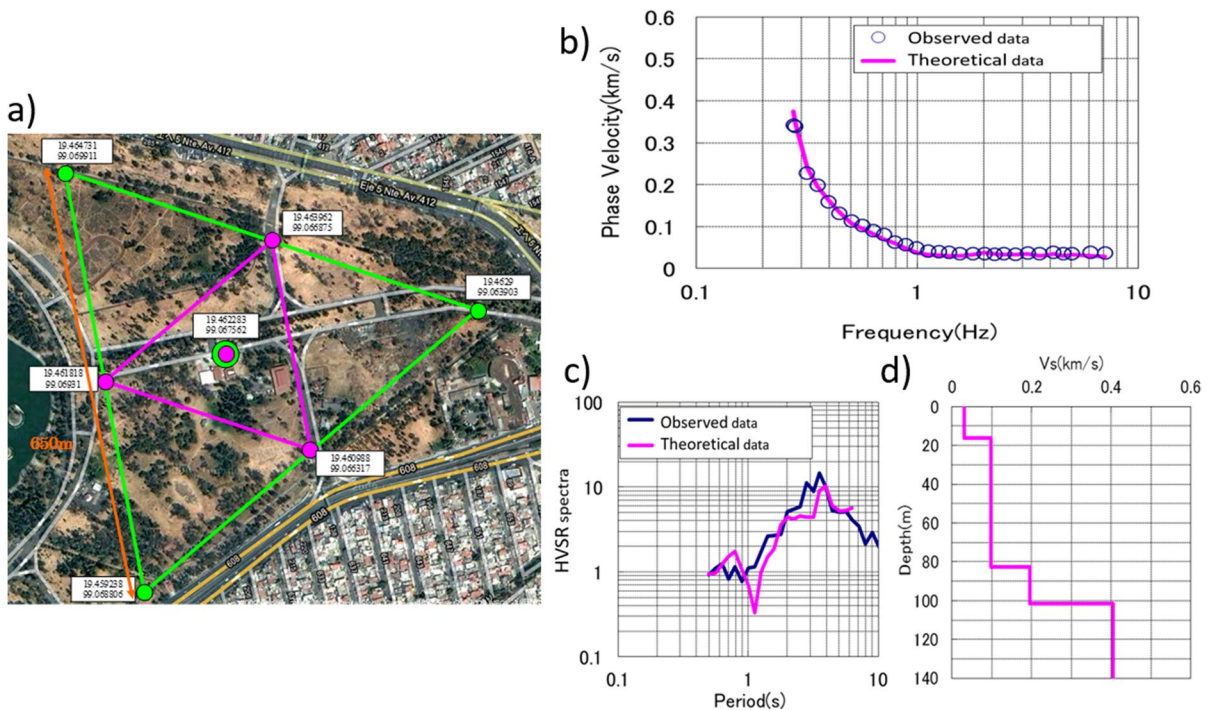


Fig. 10 Shear-wave velocity investigation in the Mexico City basin, using a passive seismic array. **a** An example of the array, **b** observed and theoretical dispersion curves, **c** observed and theoretical HVSr, and **d** an estimated V_s velocity model. A

clear peak period of 3.5 s in the HVSr spectra is due to the two shallow low-velocity layers with V_s 30 m/s and 100 m/s. (Modified from Hayashi et al. 2011)

these soft sediments has been delineated by drillhole records and microtremor measurements (Lermo and Chávez-García 1994). V_s profiles were measured by downhole seismic logging (Seo 1986) at only seven sites, and the regional V_s structure of the whole basin was not delineated. To delineate the V_s structure of the basin below central Mexico City down to a depth of approximately 200 m, three-component microtremor data were analyzed using both SPAC and HVSR (Hayashi et al. 2011) at six sites. The MAM surveys were conducted with 25- to 650-m equilateral triangular arrays (Fig. 10a). Figure 10b to d show an example of a dispersion curve, an HVSR spectrum, and a V_s model obtained in the center of the Mexico City basin. A clear dispersion curve was obtained between 0.3 and 7 Hz (Fig. 10b), and a HVSR peak was observed at a period of 3.5 s (Fig. 10c). A joint inversion of the dispersion curve and HVSR spectrum was applied to observed data, and a V_s model down to a depth of 200 m was obtained (Fig. 10d). Low-velocity layers with V_s approximately 30 and 100 m/s existed to depths of approximately 20 and 80 m, respectively. It seems that the peak period of 3.5 s in the HVSR spectra is due to the two shallow low-velocity layers with V_s of 30 and 100 m/s, respectively.

The direct fitting method of SPAC interpretation is illustrated using samples of microtremor data from Hollister Municipal Airport, California. The site and early microtremor surveys along with borehole data were described by Liu et al. (2000). This paper uses data acquired in a later survey with pairs of nested triangles (see example in Fig. 2b), where the triangle side lengths range from 12.5 to 100 m, supplemented by asymmetric linear arrays placed along runway margins. Figure 11a shows the location of triangular arrays at Hollister Airport, and Fig. 11 shows as an example the observed and model coherency spectra acquired with the triangle of side length 50 m; it is evident that useful data exist over a bandwidth of 2 to 17 Hz for spatial averaging of coherencies over the three radial separations ($r=28.8$ m), and 2 to 12 Hz for averaging over the side lengths ($r=50$ m). Section 11 illustrates how this methodology may be extended to cases where the arrays are not symmetric.

Further case studies integrating use of SPAC methods and HVSR spectra are provided in AH18 (Sections 7 to 9) and elsewhere in the literature (e.g., Stephenson et al. 2009; Suzuki and Yamanaka 2010;

Zor et al. 2010; Hayashi et al. 2011; Asten et al. 2014; Hayashi and Craig 2017; Chieppa et al. 2020).

The challenge of using passive microtremor methods to correctly detect and quantify low-velocity layers (LVL) situated below overlying higher-velocity sediments is difficult. Surface-wave models are subject to non-uniqueness limitations; the blind trial reported by Garofalo et al. (2016a) included one site (Grenoble, glacial sediments) having a 10-m-thick layer of soft clay under 25 m of surficial sands and gravels. The blind trial showed only four of 14 groups correctly identified presence of the LVL. Roberts and Asten (2004) describe a site where an LVL of 25 m of Quaternary alluvial deposits beneath 12 m of Quaternary basalts was resolved by SPAC methods. Farrugia et al. (2016) quantified thicknesses of 20 to 50 m of soft clays below 10 to 50 m of hard surficial limestones. Teague et al. (2018) resolved multiple layers of sand interbedded with gravels over a total thickness of 150 m, aided by geological control. AH18 contains additional discussion of the LVL challenge for microtremor methods.

10 Advanced approaches

Where logistics and instrument availability permit, dense arrays comprising circles of stations with five or more stations per circle are highly effective. Array processing using FK methods gives precise results with such arrays and has the advantage that in the presence of directional seismic noise and/or departures from symmetry in the array geometry the MAM method remains robust. Foti et al. (2017) provide a tutorial explanation of FK methods, and a set of detailed examples is given in Poggi et al. (2017).

With less dense arrays, typically used where logistical and instrumental constraints place limits on the complexity of array geometry, both the above advantages cease to exist. In addition, site access or corruption of the microtremor signal by local noise in the vicinity of a sensor may reduce a nested triangle array to an asymmetrical shape. In order to gain useful SPAC spectra from such arrays, a variant termed krSPAC (Asten et al. 2019b; Stephenson et al. 2019; Asten 2021a, b) may be used. The concept behind the krSPAC approach is that if the frequency axis of coherency curves is transformed to the dimensionless scale kr (where k is wavenumber and r is separation of

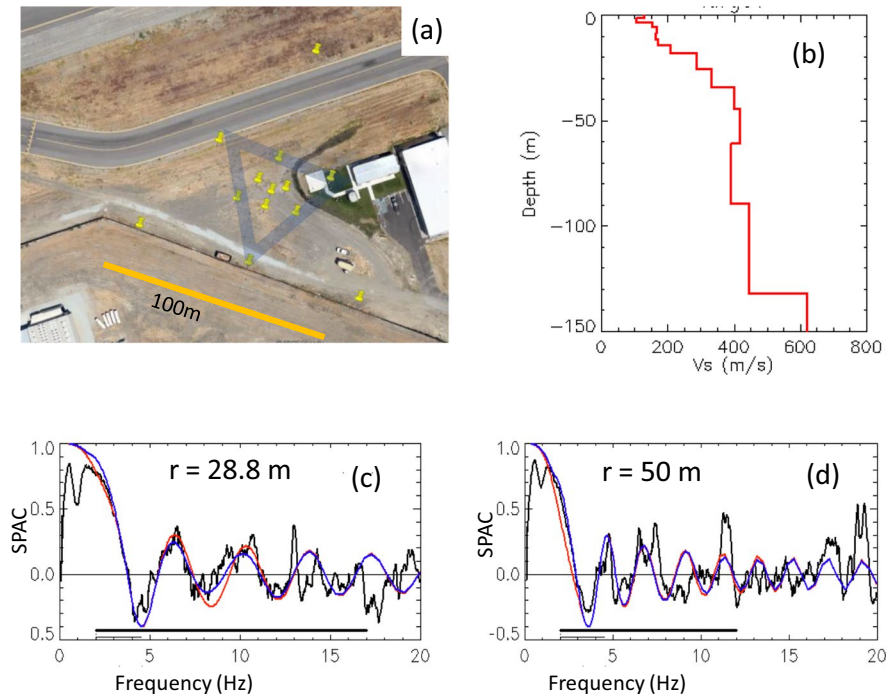


Fig. 11 **a** Locality for MAM triangular arrays at Hollister Municipal Airport, California. Center of the array is at 36.888543°N 121.413778°W. Yellow pins show four nested triangles. Blue shading shows one triangle side length 50 m used for this figure. **b** V_s profile interpreted from all arrays, including larger arrays shown in Fig. 12, using geological data provided in Liu et al. (2000). **c**, **d** SPAC spectra for triangle radii and sides with interstation distances $r=28.8$ and 50 m,

respectively. Black line—observed SPAC; red and blue lines—model SPAC spectra for the fundamental Rayleigh mode R_0 and the effective mode R_e . The fitting is performed by least squares using the observed and model R_e curves. Thick black line—the frequency range used in the curve fitting. The radial distance recovers useful data over a frequency band 2 to 17 Hz. Side length distance likewise over band 2 to 12 Hz

pairs of stations), coherency curves can be averaged for multiple pairs of stations regardless of whether the pairs have different spacings. Details of the method are given in Asten et al. (2019b) and Stephenson et al. (2019).

Figure 12 shows how the krSPAC approach allows direct fitting to be used on an asymmetric array produced by the logistical restriction of access to runway margins at the Hollister Airport (Fig. 12a). Acquisition instrumentation was a set of 2-Hz geophones wired to a multichannel seismograph. Apart from geometrical constraints, data at many stations are partially corrupted by noise presumed to be from industrial machinery or signaling, dominant at frequencies 1.3 and 1.7 Hz. After review of noise characteristics at various stations, we selected an asymmetric four-station triangle as shown in Fig. 12a, having unequal “radii” (292, 156, 151 m) and unequal side lengths (364, 307, 295 m) to develop the V_s model shown in Fig. 12b. Figure 12c and e show the

conventional SPAC direct fitting, with the layered earth model being very close to one of the models hypothesized in Fig. 11 (curve 5) in Liu et al. (2000). The spatial averaging used in the conventional method fails due to the unequal station spacing, for frequencies above about 2 Hz, giving meaningless results at these higher frequencies. However, when spatial averaging is performed in the kr domain, meaningful fitting of observed data to model data is achieved over frequency ranges up to 4 and 3 Hz, respectively, for spatial averaging over the three notional “radii” and over the three side lengths (Fig. 12d, f).

11 Lessons from the COSMOS blind trials 2018–2020

The COSMOS blind trials of MAM methods involved 34 groups of analysts using about 13 different software

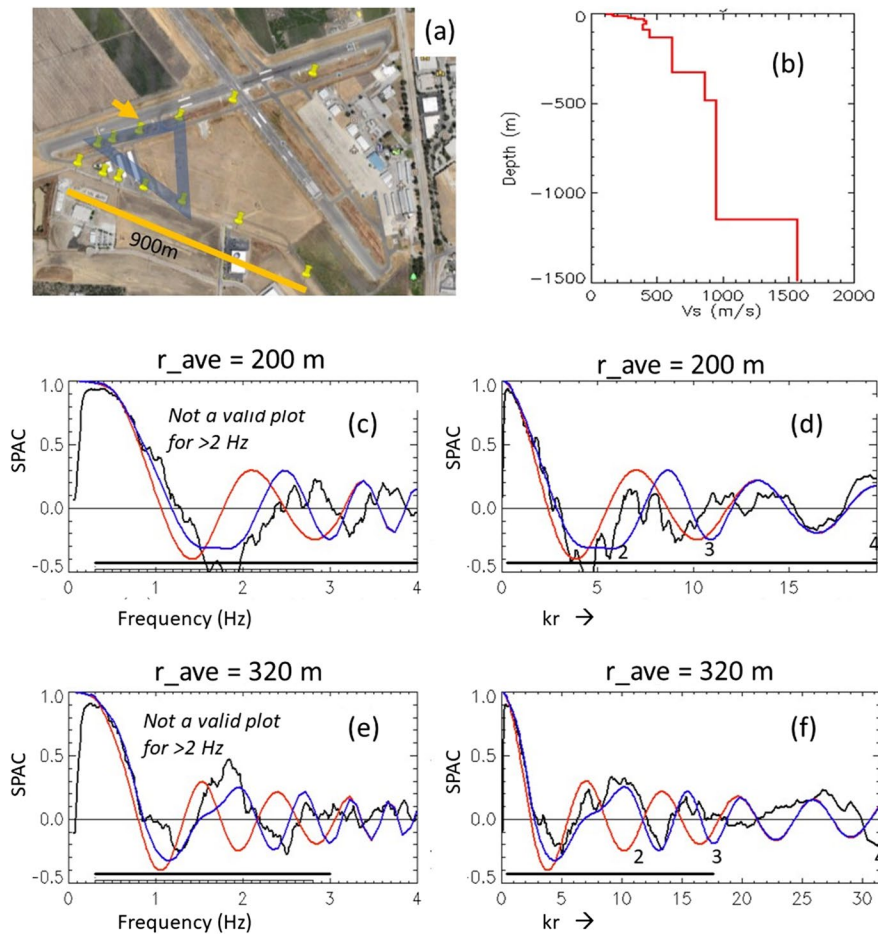


Fig. 12 **a** Locality for large asymmetric array at Hollister Municipal Airport, California. Yellow pins show geophone positions. Blue asymmetric “triangle” shows a four-station triangle selected for krSPAC interpretation. Yellow arrow shows the station selected as a notional “center” for purposes of constructing unequal “radial” distances to each vertex of the blue triangle. **b** V_s profile interpreted using data from Liu et al (2000) and this study (see also Fig. 11b). **c**, **e** Conventional SPAC spectra for asymmetric blue triangle; averaged “radial” and averaged side length distances $r_{ave} = 200, 322$ m respectively. The large variation in inter-station distances used in the spatial averages makes the conventional SPAC plots of dubious value for frequencies above 2 Hz. Black line—observed SPAC; red and blue lines—model SPAC spectra for the fundamental

Rayleigh mode R_0 and the effective mode R_e . The fitting is performed by least squares using the observed and model R_e curves. **d**, **f** SPAC plots obtained using the krSPAC algorithm where coherencies for pairs of unequally spaced stations are averaged in dimensionless wavenumber space kr rather than in frequency space (as described in Asten et al., 2018). Annotations above the kr axis are equivalent frequencies. Thick black line—the frequency range used in the curve fitting of observed SPAC and modeled SPAC computed from R_e . The “radial” distances **d** recover useful data over a frequency band 0.3 to 4 Hz. The side length distances **f** give useful data over the band 0.3 to 3 Hz. The standard deviation of observed and model R_e data improves from 0.14 for conventional SPAC in **e** to 0.10 for krSPAC in **f**

packages to perform blind interpretations on MAM array data from four different sites in the USA, Canada, and Europe (Asten et al. 2019a; 2021a). For each site, the array data were released to analysts in four phases, allowing objective analysis of the usefulness of simple two-station arrays, sparse arrays (simple triangles), and

dense arrays (circles or nested triangles). The final phase was reinterpretation and reconciliation of the geophysical data with all available geological information. The phase 1 results illustrated the dangers of erroneous interpretations of V_s when using two-station arrays in the presence of directional seismic noise. Our conclusion is

that we recommend in Section 6.2 against use of such two-station arrays if it can be avoided.

The phase 2 trials (sparse triangular arrays) showed that a majority of analysts were able to get acceptable V_s profiles where the goal was time-averaged V_s data (V_{S10} , V_{S30} , or V_{S100}) for the site as required for general earthquake hazard codes (e.g., BSSC, 2003). However, such data were not sufficient where depth to major interfaces (e.g., base of surficial soft sediments or depth to basement rock) are required.

The phase 3 trials using dense 2D arrays demonstrated that accurate interpretation of depth to interfaces from MAM surveys requires the use of dense or multiple arrays and the use of three-component data to allow HVSR data to be used in conjunction with phase velocity dispersion data. Section 9 and Fig. 9 of this paper illustrate this process.

The blind trials did not identify any MAM software package as clearly superior; for example, the top six analysts assessing time-averaged V_s data used five different software systems. Analysts' practice and skill were deemed important. To facilitate training in these skills, the blind trial data are available in the four phases and thus are a tool for future education in MAM interpretation (Asten et al. 2021b).

Opinion among analysts was split based on the question of whether active surface wave methods should be employed in order to define the V_s profile for near surface (e.g., upper ~ 10 m) of topsoil. Near surface definition requires high-frequency Rayleigh-wave dispersion data, typically above 10 Hz. The blind trials demonstrated that the widest useable bandwidths of microtremor data were obtained by analysts using the ESAC method and with the MMSPAC method based on direct fitting of coherency spectra; it is arguable that maximizing the useable bandwidth in passive seismic methods up to 20–30 Hz removes the need for supplementary active surface-wave measurements (e.g., Hayashi et al. 2016).

The last of these points is illustrated in the present paper. Generally, with low-noise data and an absence of lateral variations in geology, the observed SPAC curve can be interpreted to a high-frequency limit of about the third minimum of the plot (see e.g., Fig. 11c). This minimum corresponds to a wavelength of order $0.4r$, where r is the minimum sensor separation in the array.

12 Conclusions

This paper summarized fundamental theory of the microtremor array method and provided general guidelines for data acquisition and processing. The results of several blind tests have demonstrated that MAM can provide reliable investigation results applicable for engineering purposes. We recommend that surveys should ideally use isotropic arrays (e.g., circular or triangular), or at least 2D arrays (e.g., L-shape), with the maximum receiver spacing being larger than the desired investigation depth. Various phase velocity calculation and inversion methods have strengths and weaknesses, and no method is conclusively superior to other methods. We recommend applying several different methods to the same data and comparing the resulting velocity models. The inversion of dispersion curves is essentially non-unique. It is important to understand that the results include uncertainty, and practitioners should try to incorporate other information in processing and interpretation to mitigate uncertainty to the extent possible. Applicability of the method and quality of data are very dependent on the site conditions, and we caution that the MAM is not applicable everywhere. We recommend initial processing of data immediately after data collection to verify that the raw data include sufficient coherent information. Unlike active seismic methods, the raw passive data of MAM look like noise, and it is difficult to evaluate data quality without spectral and/or coherency analysis. The calculation of phase velocity from ambient noise is not intuitive compared with other seismic methods. An understanding of fundamental theory and a sharing of experimental knowledge are important to ensure accuracy and reliability of the results of such investigations.

Acknowledgements The Consortium of Organizations for Strong Motion Observation Systems (COSMOS) consisting of the US Geological Survey, the Geological Survey of Canada, and a group of North American power companies, consisting of Southern California Edison and Pacific Gas and Electric, identified the need for these blind trials, for these guidelines for best-practices and provided funding and encouragement to facilitate the project. This material is also based upon work supported by the US Geological Survey under Cooperative Agreement No. G17AC00058. The views and conclusions contained in this document are those of the authors and should not be interpreted as representing the opinions or policies of the US Geological Survey. Mention of trade names or commercial products does not constitute their endorsement by the US

Geological Survey. Any use of trade, product, or firm names is for descriptive purposes only and does not imply endorsement by the US Government, the Canadian Government, or COSMOS. This paper is Natural Resources of Canada contribution number 20200665.

Open Access publication fees for this paper were directly funded by COSMOS.

Data from Hollister Municipal Airport were acquired by Geometrics, Inc. as part of an internal project and are used here by permission of Geometrics, Inc.

Funding Funding to assist with the preparation of this manuscript was provided by the U.S. Geological Survey.

Declarations

Conflict of interest The authors declare no competing interests.

Disclaimer Any use of trade, firm, or product names is for descriptive purposes only and does not imply endorsement by the US Government.

Open Access This article is licensed under a Creative Commons Attribution 4.0 International License, which permits use, sharing, adaptation, distribution and reproduction in any medium or format, as long as you give appropriate credit to the original author(s) and the source, provide a link to the Creative Commons licence, and indicate if changes were made. The images or other third party material in this article are included in the article’s Creative Commons licence, unless indicated otherwise in a credit line to the material. If material is not included in the article’s Creative Commons licence and your intended use is not permitted by statutory regulation or exceeds the permitted use, you will need to obtain permission directly from the copyright holder. To view a copy of this licence, visit <http://creativecommons.org/licenses/by/4.0/>.

Appendix 1

This appendix summarizes the essential features of the SPAC method. Let us start with two traces $f(t)$ and $g(t)$ obtained at two receives with separation Δx . For the sake of simplicity, waves are propagating parallel to a receiver array (Fig. 13a). Two traces are transformed into frequency domain and written as $F(\omega)$ and $G(\omega)$. Cross-correlation of the two traces ($CC_{fg}(\omega)$) can be defined as:

$$CC_{fg}(\omega) = F(\omega) \cdot \overline{G(\omega)} = A_f(\omega)A_g(\omega) \cdot \exp^{i\Delta\phi(\omega)} \quad (6)$$

where $A_f(\omega)$ and $A_g(\omega)$ are amplitude of $F(\omega)$ and $G(\omega)$, respectively. Phase velocity $c(\omega)$ is directly related to the phase difference $\Delta\phi(\omega)$.

$$\Delta\phi(\omega) = \frac{\omega \cdot \Delta x}{c(\omega)} \quad (7)$$

Using Eq. (7), Eq. (6) can be rewritten as,

$$CC_{fg}(\omega) = F(\omega) \cdot \overline{G(\omega)} = A_f(\omega)A_g(\omega) \cdot \exp^{i\left(\frac{\omega \cdot \Delta x}{c(\omega)}\right)} \quad (8)$$

Dividing the cross-correlation of the two traces ($CC_{fg}(\omega)$) by autocorrelations ($A_f(\omega)$ and $A_g(\omega)$) yields complex coherency of two traces $COH_{fg}(\omega)$.

$$COH_{fg}(\omega) = \frac{CC_{fg}(\omega)}{\sqrt{A_f(\omega)A_g(\omega)}}. \quad (9)$$

Using Eq. (8), Eq. (9) can be rewritten as,

$$COH_{fg}(\omega) = \frac{CC_{fg}(\omega)}{\sqrt{A_f(\omega)A_g(\omega)}} = \exp^{i\left(\frac{\omega \cdot \Delta x}{c(\omega)}\right)}, \quad (10)$$

and taking the real part of this gives

$$\text{Re}(COH_{fg}(\omega)) = \cos\left(\frac{\omega \cdot \Delta x}{c(\omega)}\right). \quad (11)$$

Equation (11) expresses the fact that the real part of the complex coherency for two traces takes the form of a cosine function. The SPAC coefficient for two-dimensional array data is defined as the directional average of complex coherencies Eq. (10), giving

$$SPAC(r, \omega) = \frac{1}{2\pi} \int_{\varphi=0}^{\varphi=2\pi} COH(r, \varphi, \omega) d\varphi, \quad (12)$$

where r is the separation of two receivers (or radius of a circle), and φ is the angular separation of the two sensors.

In essence, Eq. (12) calculates the complex coherencies for two sensors with separation r and angular separation φ and it averages these coherencies around a circle (Fig. 13b). The directional average of trigonometric functions reduces to a Bessel function as shown by Okada (2003):

$$J_0(kr) = \frac{1}{2\pi} \int_{\varphi=0}^{\varphi=2\pi} \cos(kr, \varphi) d\varphi, \quad (13)$$

where k is the wave number.

Figure 14 compares cosine functions corresponding to sensor pairs between the center and receivers A to G with orientation φ as shown in Fig. 13, and

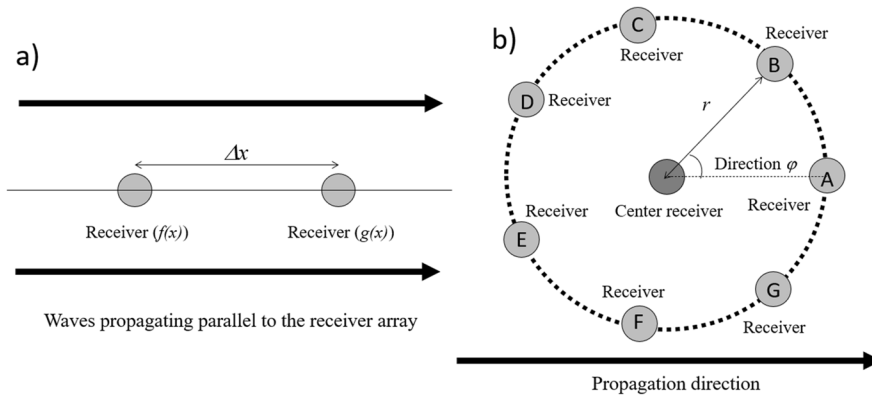


Fig. 13 Spatial auto-correlation in 1D (a) and 2D (b). In the 1D wave propagation (a), waves propagate parallel to the receiver array, and cross-correlation between two receivers goes to cosine function. In the 2D array (b), cross-correlations

Bessel functions. Using Eq. (13), the directional average of the right side of Eq. (12) can be written as.

$$J_0\left(\frac{\omega \cdot r}{c(\omega)}\right) = \frac{1}{2\pi} \int_{\varphi=0}^{\varphi=2\pi} \cos\left(\frac{\omega \cdot r}{c(\omega)}, \varphi\right) d\varphi, \quad (14)$$

Finally, Eqs. (12) and (14) can be combined to get

$$\text{Re}(SPAC(R, \omega)) = J_0\left(\frac{\omega}{c(\omega)} r\right), \quad (15)$$

where $c(\omega)$ is the fundamental mode of phase velocity at the angular frequency ω .

When we process surface waves, seismic interferometry (SI) is essentially the same as spatial

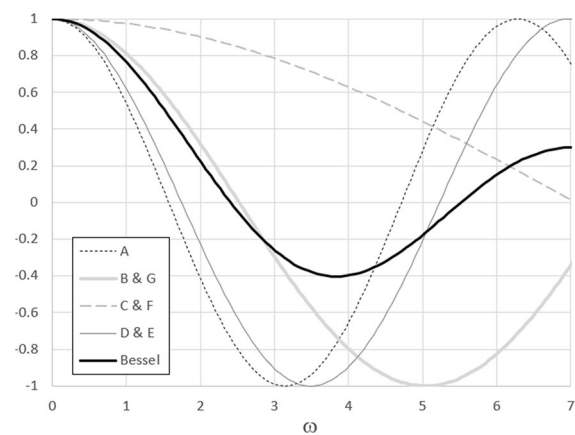


Fig. 14 Comparison of cosine ($\cos(\omega, \varphi)$) functions corresponding to sensor pairs between center and A to G with orientation φ as shown in Fig. 13 and the Bessel ($J_0(\omega)$) function

are calculated between a receiver at the middle of the circle and receivers on the circle. The directional average of cosine function goes to Bessel function as shown in Fig. 14

autocorrelation (SPAC). SPAC or coherency can be considered the real part of cross-correlation divided by autocorrelation in frequency domain. In other words, the inverse Fourier transform of SPAC corresponds to the cross-correlation in time domain. Figure 15 shows an example of SPAC in the frequency domain (Fig. 15a) and time domain (Fig. 15c) calculated from microtremors (AH18 Section 10). Figure 15b shows the error between the coherencies and Bessel functions, and phase velocities that provide minimum error were defined as a dispersion curve. Frequency-domain coherencies (Fig. 15a) were transformed to time domain by the inverse Fourier transform (Fig. 15c). The time domain data are termed the SI or cross-correlation and resemble a shot gather. Further processing using phase shift and stack (Park et al. 1999) transforms it to a phase velocity versus frequency domain plot (Fig. 15d), and phase velocities that provide maximum stacked amplitude are defined as a dispersion curve. Figure 15a–d correspond to SPAC and SI, respectively, and it is evident that the dispersion curves obtained by two methods are almost identical.

Appendix 2

This appendix describes a traditional iterative non-linear least squares method in which the number and thickness of subsurface layers are fixed through the inversion process, and the layer specific V_S is the only unknown. As an alternative, both V_S and thickness of each layer are often estimated in the inversion. V_P and

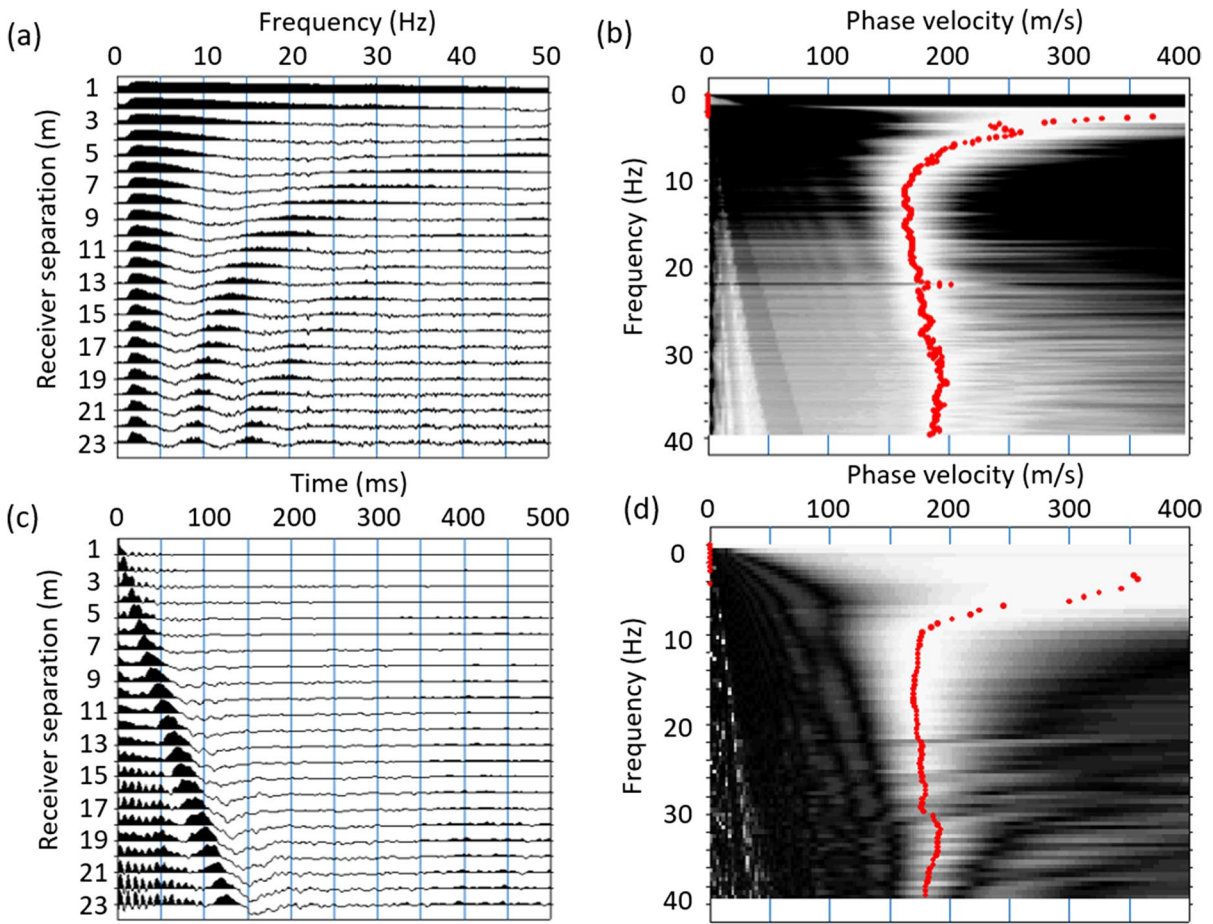


Fig. 15 **a** Example of SPAC in the frequency domain calculated from microtremor measurement. **b** Phase velocity image in the frequency domain calculated from **a**. **c** SPAC in the

time domain calculated from **a** by inverse Fourier transform. **d** Phase velocity image in the frequency domain calculated from **c**. (Modified from AH18)

density are usually related to V_S linearly with empirical equations (e.g., Kitsunezaki et al. 1990; Ludwig et al. 1970) in each step of the iteration. The computation procedure is summarized as follows.

First, the set of V_S values in each layer can be written as a one-dimensional vector \mathbf{x} , as.

$$\mathbf{x}^T = (V_{S1}, V_{S2}, \dots, V_{SM}), \tag{16}$$

where $V_{S1}, V_{S2}, \dots, V_{SM}$ are the V_S values for the 1st, 2nd, and M th layers, respectively.

As an objective function, we choose the L2 norm between the observed and calculated phase velocity values from \mathbf{x} , that is,

$$\sum_i^N (f_i^{\text{obs}} - f_i^{\text{cal}}(V_{S1}, V_{S2}, \dots, V_{SM}))^2 = \sum_i^N (f_i^{\text{obs}} - f_i^{\text{cal}}(x))^2 \rightarrow \text{Minimum} \tag{17}$$

where N is the number of observed phase velocity data, f^{obs} are phase velocities obtained from observed waveform data and f^{cal} are theoretical phase velocities for the V_S model.

A theoretical phase velocity curve can be calculated by the matrix method (e.g., Saito and Kabasawa (1993)). Now, a Jacobian matrix can be written as

$$a = \begin{pmatrix} \frac{\partial f_1^{\text{cal}}(x)}{\partial V_{S1}} & \frac{\partial f_1^{\text{cal}}(x)}{\partial V_{S2}} & \dots & \frac{\partial f_1^{\text{cal}}(x)}{\partial V_{SM}} \\ \frac{\partial f_2^{\text{cal}}(x)}{\partial V_{S1}} & \frac{\partial f_2^{\text{cal}}(x)}{\partial V_{S2}} & \dots & \frac{\partial f_2^{\text{cal}}(x)}{\partial V_{SM}} \\ \frac{\partial f_3^{\text{cal}}(x)}{\partial V_{S1}} & \frac{\partial f_3^{\text{cal}}(x)}{\partial V_{S2}} & \dots & \frac{\partial f_3^{\text{cal}}(x)}{\partial V_{SM}} \\ \dots & \dots & \dots & \dots \\ \frac{\partial f_N^{\text{cal}}(x)}{\partial V_{S1}} & \frac{\partial f_N^{\text{cal}}(x)}{\partial V_{S2}} & \dots & \frac{\partial f_N^{\text{cal}}(x)}{\partial V_{SM}} \end{pmatrix}. \tag{18}$$

We can see that the unknown vector x is in the derivatives, and it makes the inversion non-linear. One of the consequences is that an initial guess model must be constructed, which must predict the data sufficiently well to obtain convergence. In actual calculation, elements of the Jacobian matrix a are usually calculated numerically using a finite-difference method (Xia et al. 1999). A residual between observed and theoretical phase velocities can be expressed as vector y given by:

$$y^T = \begin{pmatrix} f_1^{obs} - f_1^{cal}(x) \\ f_2^{obs} - f_2^{cal}(x) \\ f_3^{obs} - f_3^{cal}(x) \\ \vdots \\ f_N^{obs} - f_N^{cal}(x) \end{pmatrix} \quad (19)$$

The correction vector Δx to a given guess for $f(x)$ can be calculated by the least squares method as follows:

$$(a^T a + \varepsilon I) \Delta x = a^T y, \quad (20)$$

where ε is a damping parameter stabilizing the inversion. In the l th iteration, a new estimated model x^{l+1} is calculated as

$$x^{l+1} = x^l + \gamma \Delta x, \quad (21)$$

where γ is the constant specifying the step length. The method used to construct the initial model (x^0) is described in Section 7.1.

Generally, the non-linear and non-unique nature of geophysical inverse problems requires the introduction of spatial regularization to converge to a physically meaningful result. In this case, it is common to regularize the variance in V_S between each layer as follows:

$$(a^T a + \alpha r_v^T r_v + \varepsilon I) \Delta x = a^T y, \quad (22)$$

where r_v is the difference between V_S of two successive layers. In matrix form, this equation can be expressed as

$$r_{v,x} = \begin{pmatrix} 1 & -1 & 0 & \cdot & 0 & 0 \\ 0 & 1 & -1 & \cdot & 0 & 0 \\ 0 & 0 & 1 & \cdot & 0 & 0 \\ \cdot & \cdot & \cdot & \cdot & \cdot & \cdot \\ 0 & 0 & 0 & \cdot & 1 & -1 \end{pmatrix} \begin{pmatrix} V_{S1} \\ V_{S2} \\ V_{S3} \\ \vdots \\ V_{SM-1} \\ V_{SM} \end{pmatrix} = \begin{pmatrix} 0 \\ 0 \\ 0 \\ 0 \\ 0 \end{pmatrix}, \quad (23)$$

where α is the weight of regularization, and large α makes an inverted model smoother.

References

- Abe K (1986) The Michoacan, Mexico earthquake of September 19, 1985: outline of source characteristics. Proceedings of the 14th Earthquake Ground Motion Symposium, p. 3–6 (in Japanese)
- Aki K (1957) Space and time spectra of stationary stochastic waves, with special reference to microtremors. Bull Earthq Res Inst 35:415–456
- Asten MW (2006) On bias and noise in passive seismic data from finite circular array data processed using SPAC methods. Geophysics 71(6):V153–V162. <https://doi.org/10.1190/1.2345054>
- Asten MW, Dhu T, Lam N (2004) Optimised array design for microtremor array studies applied to site classification — observations, results and future use. Vancouver: Proceedings of the 13th Annual World Conference of Earthquake Engineering, Paper 2903
- Asten MW, Boore DM (2005) Comparison of shear-velocity profiles of unconsolidated sediments near the Coyote borehole (CCOC) measured with fourteen invasive and non-invasive methods. In: Asten, MW, Boore DM (Eds.) Blind comparisons of shear-wave velocities at closely spaced sites in San Jose, California: U.S. Geological Survey Open-File Report 2005–1169, 35 pp. <https://doi.org/10.3133/ofr20051169>
- Asten MW, Askan A, Ekincioglu EE, Sisman FN, Ugurhan B (2014) Site characterization in northwestern Turkey based on SPAC and HVSR analysis of microtremor noise. Explor Geophys 45(2):74–85. <https://doi.org/10.1071/EG12026>
- Asten MW, Hayashi K (2018) Application of the spatial autocorrelation method for shear-wave velocity studies using ambient noise. Surv Geophys 39:633–659. <https://doi.org/10.1007/s10712-018-9474-2>
- Asten MW, Yong A, Foti S, Hayashi K, Martin AJ, Stephenson WJ, Cassidy JF, Coleman J (2019a) A preliminary assessment of uncertainties attributed by analysts, array types and processing algorithms for microtremor observations, via the COSMOS Blind Trials. ASEG Extended Abstracts 2019:1–4. <https://doi.org/10.1080/22020586.2019.12073054>
- Asten MW, Stephenson WJ, Hartzell S (2019b) Spatially averaged coherencies (krSPAC) and Rayleigh effective-mode modeling of microtremor data from asymmetric arrays. Geophysics 84(3):EN47–EN56. <https://doi.org/10.1190/geo2018-0524.1>
- Asten MW, Yong A, Foti S, Hayashi K, Martin AJ, Stephenson WJ, Cassidy JF, Coleman J, Nigbor R, Castellaro S, Chimoto K, Cornou C, Cho I, Hayashida T, Hobiger M, Kuo C-H, Macau A, Mercerat ED, Molnar S, Pananont P, Pilz M, Poovarodom N, Sáez E, Wathelet M, Yamanaka H, Yokoi T, Zhao D (2021a) An assessment of uncertainties in V_S profiles obtained from microtremor observations in

- the phased 2018 COSMOS Blind Trials. *J Seismol* this issue
- Asten MW, Stephenson WJ, Yong A, Foti S, Hayashi K, Martin AJ, Nigbor R (2021b) Data release for: an assessment of uncertainties attributed by analysts, array types and processing algorithms for microtremor observations, using the phased 2018 COSMOS Blind Trials. U.S. Geological Survey data release. <https://doi.org/10.5066/P9IA54PL>
- Asten MW (2021) Blind study site assessment of shear-wave velocity at Kumamoto City, Japan, using direct-fitting SPAC methods. Proceedings of the 6th IASPEI/IAEE International Symposium. Kyoto: The Effects of Surface Geology on Seismic Motion (ESG6), Paper 5074
- Bettig B, Bard PY, Scherbaum F, Riepl J, Cotton F, Cornou C, Hatzfeld D (2001) Analysis of dense array noise measurements using the modified spatial auto-correlation method (SPAC): application to the Grenoble area. *Bolletino Di Geofisica Teorica Ed Applicata* 42(3–4):281–304
- Boore DM, Asten MW (2008) Comparisons of shear-wave slowness in the Santa Clara Valley, California, using blind interpretations of data from invasive and non-invasive methods. *Bull Seismol Soc Am* 98(4):1983–2003. <https://doi.org/10.1785/0120070277>
- Building Seismic Safety Council (BSSC) (2003) NEHRP recommended provisions for seismic regulations for new buildings and other structures (FEMA 450), part1: provisions. Washington, D.C.: Federal Emergency Management Agency, 356 pp
- Capon J (1969) High resolution frequency wavenumber spectrum analysis. *Proc IEEE* 57(8):1408–1418. <https://doi.org/10.1109/PROC.1969.7278>
- Capon J (1973) Signal processing and frequency-wavenumber spectrum analysis for a large aperture seismic array. In: Bolt, BA (Ed.) *Methods in Computational Physics: Advances in Research and Applications*. New York: Academic Press, 13:1–59. <https://doi.org/10.1016/B978-0-12-460813-9.50007-2>
- Chávez-García F, Manakou MV, Raptakis DG (2014) Subsoil structure and site effects: a comparison between results from SPAC and HVSr in sites of complex geology. *Soil Dyn Earthq Eng* 57:133–142. <https://doi.org/10.1016/j.soildyn.2013.11.008>
- Chávez-García FJ, Manakou MV, Hollender F (2018) Site effects using methods based on lateral homogeneity and laterally heterogeneous media: an impossible marriage? *Bull Earthq Eng* 16:2729–2756. <https://doi.org/10.1007/s10518-017-0296-2>
- Chiappa D, Hobiger M, Fah D (2020) Ambient vibration analysis on seismic arrays to investigate the properties of the upper crust: an example from Herdern in Switzerland. *Geophys J Int* 222(1):526–543. <https://doi.org/10.1093/gji/ggaa182>
- Cho I, Senna S, Fujiwara H (2013) Miniature array analysis of microtremors. *Geophysics* 78(1):KS13–KS23. <https://doi.org/10.1190/geo2012-0248.1>
- Cho I (2020) Two-sensor microtremor SPAC method: potential utility of imaginary spectrum components. *Geophys J Int* 220(3):1735–1747. <https://doi.org/10.1093/gji/ggz454>
- Claproud M, Asten MW, Kristek J (2011) Using the SPAC microtremor method to identify 2D effects and evaluate 1D shear-wave velocity profile in valleys. *Bull Seismol Soc Am* 101(2):826–847. <https://doi.org/10.1785/0120090232>
- Claproud M, Asten MW, Kristek J (2012) Combining HVSr microtremor observations with the SPAC method for site resonance study of the Tamar Valley in Launceston (Tasmania, Australia). *Geophys J Int* 191(2):765–780. <https://doi.org/10.1111/j.1365-246X.2012.05654.x>
- Cornou C, Ohrnberger M, Boore DM, Kudo K, Bard P-Y (2007) Derivation of structural models from ambient vibration array recordings: results from an international blind test. In: Bard P-Y, Chaljub E, Cornou C, Gueguen P (Eds.) *Grenoble: Third International Symposium on the Effects of Surface Geology on Seismic Motion (ESG2006)*, p. 1127–1215
- Farrugia D, Paolucci E, D’Amico S, Galea P (2016) Inversion of surface wave data for subsurface shear wave velocity profiles characterized by a thick buried low-velocity layer. *Geophys J Int* 206(2):1221–1231. <https://doi.org/10.1093/gji/ggw204>
- Foti S, Hollender S, Garofalo F, Albarello D, Asten M, Bard P-Y, Comina C, Cornou C, Cox B, Di Giulio G, Forbriger T, Hayashi K, Lunedei E, Martin A, Mercerat D, Ohrnberger M, Poggi V, Renalier F, Sicilia D, Socco LV (2017) Guidelines for the good practice of surface wave analysis: a product of the InterPACIFIC project. *Bull Earthq Eng* 16:2367–2420. <https://doi.org/10.1007/s10518-017-0206-7>
- Garofalo F, Foti S, Hollender F, Bard PY, Cornou C, Cox BR, Ohrnberger M, Sicilia D, Asten M, Di Giulio G, Forbriger T, Guillier B, Hayashi K, Martin A, Matsushima S, Mercerat D, Poggi V, Yamanaka H (2016a) InterPACIFIC project: comparison of invasive and non-invasive methods for seismic site characterization. Part I: Intra-comparison of surface wave methods. *Soil Dyn Earthq Eng* 82:222–240. <https://doi.org/10.1016/j.soildyn.2015.12.010>
- Garofalo F, Foti S, Hollender F, Bard PY, Cornou C, Cox BR, Dechamp A, Ohrnberger M, Perron V, Sicilia D, Teague D, Vergnault C (2016b) InterPACIFIC project: comparison of invasive and non-invasive methods for seismic site characterization. Part II: inter-comparison between surface-wave and borehole methods. *Soil Dyn Earthq Eng* 82:241–254. <https://doi.org/10.1016/j.soildyn.2015.12.009>
- Hayashi K (2009) Effect of array shape on the spatial auto-correlation analysis of micro-tremor array measurements. *Proc Symp Appl Geophys Eng Environ Probl* 2009:616–625. <https://doi.org/10.4133/1.3176749>
- Hayashi K (2019) Near-surface engineering. In: Nakata N, Gualtieri L and Fichtner A (Eds.) *Seismic Ambient Noise*, Cambridge: Cambridge University Press, p. 302–337. <https://doi.org/10.1017/9781108264808.012>
- Hayashi K, Inazaki T, Suzuki H (2006) Buried incised channels delineation using microtremor array measurements at Soka and Misato Cities in Saitama Prefecture. *Bull Geol Surv Japan* 57(9/10):309–325. (in Japanese) <https://doi.org/10.9795/bullgsj.57.309>
- Hayashi K, Nozu A, Tanaka M, Suzuki H, Ovando SE (2011) Joint inversion of three component microtremor measurements and microtremor array measurements at Mexico

- City. SEG Tech Prog Expand Abstracts 2011:917–921. <https://doi.org/10.1190/1.3628222>
- Hayashi K, Cakir R, Walsh TJ (2016) Comparison of dispersion curves obtained by active and passive surface wave methods: examples from seismic site characterization surveys for school seismic safety evaluations in Thurston County, Washington. Proc Symp Appl Geophys Eng Environ Probl 2016:475–483. <https://doi.org/10.4133/SAGEEP.29-081>
- Hayashi K, Craig M (2017) S-wave velocity measurement and the effect of basin geometry on site response, east San Francisco Bay area, California, USA. Phys Chem Earth 98:49–61. <https://doi.org/10.1016/j.pce.2016.07.001>
- Ikeda T, Matsuoka T, Tsuji T, Hayashi K (2012) Multimode inversion with amplitude response of surface waves in the spatial autocorrelation method. Geophys J Int 190(1):541–552. <https://doi.org/10.1111/j.1365-246X.2012.05496.x>
- Kitsunezaki C, Goto N, Kobayashi Y, Ikawa T, Horike M, Saito T, Kurota T, Yamane K, Okuzumi K (1990) Estimation of P- and S- wave velocities in deep soil deposits for evaluating ground vibrations in earthquake. Sizen-Saigai-Kagaku 9(3):1–17. (in Japanese)
- Lermo J, Chávez-García FJ (1994) Site effect evaluation at Mexico City: dominant period and relative amplification from strong motion and microtremor records. Soil Dyn Earthq Eng 13(6):413–423. [https://doi.org/10.1016/0267-7261\(94\)90012-4](https://doi.org/10.1016/0267-7261(94)90012-4)
- Liu H-P, Boore DM, Joyner WB, Oppenheimer DH, Warrick RE, Zhang W, Hamilton JC, Brown LT (2000) Comparison of phase velocities from array measurements of Rayleigh waves associated with microtremor and results calculated from borehole shear-wave velocity profiles. Bull Seismol Soc Am 90(3):666–678. <https://doi.org/10.1785/0119980186>
- Louie JN (2001) Faster, better: shear-wave velocity to 100 meters depth from refraction microtremor arrays. Bull Seismol Soc Am 91(2):347–364. <https://doi.org/10.1785/0120000098>
- Louie JN, Pancha A, Kissane B (2021) Guidelines and pitfalls of refraction microtremor surveys. J Seismol this issue
- Ludwig WJ, Nafe JE, Drake CL (1970) Seismic refraction. In: Maxwell AE (Ed.) The Sea, Vol. 4, Part 1. New York: Wiley-Interscience, p. 53–84
- Maranò S, Hobiger M, Bergamo P, Fäh D (2017) Analysis of Rayleigh waves with circular wavefront: a maximum likelihood approach. Geophys J Int 210(3):1570–1580. <https://doi.org/10.1093/gji/ggx225>
- Menke W (1984) Geophysical data analysis: discrete inverse theory. New York: Academic Press. <https://doi.org/10.1016/C2011-0-69765-0>
- Molnar S, Cassidy JF, Castellaro S, Cornou C, Crow H, Hunter JA, Matsushima S, Sanchez-Sesma FJ, Yong A (2018) Application of MHVSR for site characterization: state-of-the-art. Surv Geophys 39:613–631. <https://doi.org/10.1007/s10712-018-9464-4>
- Molnar S, Sirohey A, Bard P-Y, Castellaro S, Cornou C, Cox B, Guillier B, Hassani B, Kawase H, Matsushima S, Sánchez-Sesma FJ, Yong A (2021) A review of the microtremor horizontal-to-vertical spectral ratio (MHVSR) method. J Seismol this issue
- Obuchi T, Yamamoto H, Sano T, Saito T (2004) Estimation of underground velocity structure based on both fundamental and higher modes of Rayleigh wave in microtremors at Morioka area. Proceedings of the 111th Society of Exploration Geophysicists of Japan International Symposium p. 25–28 (in Japanese)
- Okada H, Ishikawa K, Sasabe K, Ling S (1997) Estimation of underground structures in the Osaka-Kobe area by array-network observations of microtremors. Proceedings of the 97th Society of Exploration Geophysicists of Japan Conference, p. 435–439
- Okada H (2003) The microtremor survey method. Society of Exploration Geophysicists Monograph Series 12: Tulsa, Oklahoma. <https://doi.org/10.1190/1.9781560801740.fm>
- Okada H (2006) Theory of efficient array observations of microtremors with special reference to the SPAC method. Explor Geophys 37(1):73–85. <https://doi.org/10.1071/EG06073>
- Park CB, Miller RD, Xia J (1999) Multimodal analysis of high frequency surface waves. Proceedings of the 12th EEGS Symposium on the Application of Geophysics to Engineering and Environmental Problems 115–121. https://doi.org/10.3997/2214-4609-pdb.202.1999_013
- Poggi V, Burjanek J, Fäh D (2017) Seismic site-response characterization of high-velocity sites using advanced geophysical techniques: application to the NAGRA-Net. Geophys J Int 210(2):645–659. <https://doi.org/10.1093/gji/ggx192>
- Roberts JC, Asten MW (2004) Resolving a velocity inversion at the geotechnical scale using the microtremor (passive seismic) survey method. Explor Geophys 35:14–18. <https://doi.org/10.1071/EG04014>
- Roberts J, Asten M (2008) A study of near source effects in array based (SPAC) microtremor surveys. Geophys J Int 174(1):159–177. <https://doi.org/10.1111/j.1365-246X.2008.03729.x>
- Saifuddin S, Yamanaka H, Chimoto K (2018) Variability of shallow soil amplification from surface-wave inversion using the Markov-chain Monte Carlo method. Soil Dyn Earthq Eng 107:141–151. <https://doi.org/10.1016/j.soildyn.2018.01.014>
- Saito M, Kabasawa H (1993) Computation of reflectivity and surface wave dispersion curves for layered media 2. Rayleigh Wave Calculations Butsuri-Tansa 46:283–298. (in Japanese)
- Salloum N, Jongmans D, Cornou C, Youssef Abdel Massih D, Hage Chehade F, Voisin C, Mariscal A (2014) The shear wave velocity structure of the heterogeneous alluvial plain of Beirut (Lebanon): combined analysis of geophysical and geotechnical data. Geophys J Int 199(2):894–913. <https://doi.org/10.1093/gji/ggu294>
- Schramm KA, Abbott RE, Asten MW, Bilek S, Pancha A, Patton HJ (2012) Broadband Rayleigh-wave dispersion curve and shear wave velocity structure for Yucca Flat Nevada. Bull Seismol Soc Am 102(4):1361–1372. <https://doi.org/10.1785/0120110296>
- Seo K (1986) Interpretation of strong ground motion record based on underground structure. 14th Earthquake Ground Motion Symposium, p. 63–68 (in Japanese)
- Smith NRA, Reading AM, Asten MW, Funk CW (2013) Constraining depth to basement for mineral exploration using

- microtremor: a demonstration study from remote inland Australia. *Geophysics* 78(5):B227–B242. <https://doi.org/10.1190/geo2012-0449.1>
- Socco LV, Strobbia C (2004) Surface-wave method for near-surface characterization: A tutorial. *Near surface geophysics* 2(4):165–185
- Stephenson WJ, Louie JN, Pullammanappallil S, Williams RA, Odum JK (2005) Blind shear-wave velocity comparison of ReMi and MASW results with boreholes to 200 m in Santa Clara Valley: implications for earthquake ground-motion assessment. *Bull Seismol Soc Am* 95(6):2506–2516. <https://doi.org/10.1785/0120040240>
- Stephenson WJ, Hartzell S, Frankel AD, Asten MW, Carver DL, Kim WY (2009) Site characterization for urban seismic hazards in lower Manhattan New York City, from Microtremor Array Analysis. *Geophys Res Lett* 36(3):L03301. <https://doi.org/10.1029/2008GL036444>
- Stephenson WJ, Asten MW, Odum JK, Frankel AD (2019) Shear-wave velocity in the Seattle basin to 2 km depth characterized with the krSPAC microtremor array method: insights for urban basin-scale imaging. *Seismol Res Lett* 90(3):1230–1242. <https://doi.org/10.1785/0220180194>
- Suzuki H, Yamanaka H (2010) Joint inversion using earthquake ground motion records and microtremor survey data to S-wave profile of deep sedimentary layers. *Butsuri-Tansa* 63(3):215–227. (in Japanese) <https://doi.org/10.3124/segj.63.215>
- Teague D, Cox B, Bradley B, Wotherspoon L (2018) Development of deep shear wave velocity profiles with estimates of uncertainty in the complex interbedded geology of Christchurch. *New Zealand Earthquake Spectra* 34(2):639–672. <https://doi.org/10.1193/041117eqs069m>
- Wapenaar K (2004) Retrieving the elastodynamic Green's function of an arbitrary inhomogeneous medium by cross correlation. *Phys Rev Lett* 93(25):254301. <https://doi.org/10.1103/PhysRevLett.93.254301>
- Wathelet M, Guillier B, Roux P, Cornou C, Ohrnberger M (2018) Rayleigh wave three-component beamforming: signed ellipticity assessment from high-resolution frequency-wavenumber processing of ambient vibration arrays. *Geophys J Int* 215(1):507–523. <https://doi.org/10.1093/gji/ggy286>
- Xia J, Miller RD, Park CB (1999) Estimation of near-surface shear-wave velocity by inversion of Rayleigh waves. *Geophysics* 64(3):691–700. <https://doi.org/10.1190/1.1444578>
- Yamamoto H (2000) An experiment for estimating phase velocities of Love waves from three-component microtremor array observations. *Butsuri-Tansa* 53:153–166. (in Japanese)
- Yamanaka H, Ishida J (1996) Application of genetic algorithms to an inversion of surface-wave dispersion data. *Bull Seismol Soc Am* 86(2):436–444
- Zhang H, Pankow KL, Stephenson W (2019) A Bayesian Monte Carlo inversion of spatial auto-correlation (SPAC) for near-surface V_s structure applied to both broad-band and geophone data. *Geophys J Int* 217(3):2056–2070. <https://doi.org/10.1093/gji/ggz136>
- Zhang H, Pankow KL (2021) High-resolution Bayesian spatial autocorrelation (SPAC) quasi-3-D V_s model of Utah FORGE site with a dense geophone array. *Geophys J Int* 225(3):1605–1615. <https://doi.org/10.1093/gji/ggab049>
- Zor E, Ozalaybey S, Karaaslan A, Tapırdamaz MC, Ozalaybey SC, Tarancıoğlu A, Erkan B (2010) Shear wave velocity structure of the Izmit Bay area (Turkey) estimated from active–passive array surface wave and single-station microtremor methods. *Geophys J Int* 182(3):1603–1618. <https://doi.org/10.1111/j.1365-246X.2010.04710.x>

Publisher's note Springer Nature remains neutral with regard to jurisdictional claims in published maps and institutional affiliations.